

**NASA
Technical
Paper
2225**

March 1984

NASA
TP
2225
c.1



**Experimental and Theoretical
Deposition Rates From
Salt-Seeded Combustion Gases
of a Mach 0.3 Burner Rig**

Gilbert J. Santoro,
Fred J. Kohl,
Carl A. Stearns,
Süleyman A. Gökoğlu,
and Daniel E. Rosner

LOAN COPY: RETURN TO
AFWL TECHNICAL LIBRARY
KIRTLAND AFB, N.M. 87117

LOAN COPY: RETURN TO
AFWL TECHNICAL LIBRARY
KIRTLAND AFB, N.M. 87117

NASA



**NASA
Technical
Paper
2225**

1984

**Experimental and Theoretical
Deposition Rates From
Salt-Seeded Combustion Gases
of a Mach 0.3 Burner Rig**

Gilbert J. Santoro,
Fred J. Kohl, and
Carl A. Stearns

*Lewis Research Center
Cleveland, Ohio*

Süleyman A. Gökoğlu

*Analex Corporation
Cleveland, Ohio*

Daniel E. Rosner

*Yale University
New Haven, Connecticut*



National Aeronautics
and Space Administration

Scientific and Technical
Information Branch

Summary

Deposition rates on platinum-rhodium cylindrical collectors rotating in the cross streams of the combustion gases of a salt-seeded Mach 0.3 burner rig were determined. The collectors were internally air cooled so that their surface temperatures could be widely varied while they were exposed to constant combustion gas temperatures.

The deposition rates were compared with those predicted by the chemically frozen boundary layer (CFBL) computer program, which is based on multi-component vapor transport through the boundary layer. Excellent agreement was obtained between theory and experiment for the NaCl-seeded case, but the agreement lessened as the seed was changed to synthetic sea salt, NaNO_3 , and K_2SO_4 , respectively, and was particularly poor in the case of Na_2SO_4 . However, when inertial impaction was assumed to be the deposition mechanism for the Na_2SO_4 case, the predicted rates agreed well with the experimental rates. The former were calculated from a mean particle diameter that was derived from the measured initial droplet size distribution of the solution spray.

Critical experiments showed that liquid-phase deposits were blown off the smooth surface of the platinum-rhodium collectors by the aerodynamic shear forces of the high-velocity combustion gases but that rough or porous surfaces retained their liquid deposits.

Introduction

Hot corrosion is a life-limiting form of accelerated environmental attack that can occur on vanes and blades in the hot sections of gas turbine engines (refs. 1 and 2). Over the past 15 years much progress has been made toward understanding many important features of this corrosion process. Thus it is generally agreed that deposits of sodium sulfate, often in synergistic combination with low levels of elements such as potassium, vanadium, carbon, lead, and particles or vapors of sodium chloride, are capable of compromising the protective oxide scales formed on engine components and of sometimes preventing their reformation (ref. 3). The corrosion-causing elements enter with the air ingested into the turbine inlet and with fuel. For example, turbines operating near the sea coast, on ships, or on aircraft operating close to the ocean surface can ingest Na_2SO_4 directly as a component of sea water, or NaCl in the sea water can react with the sulfur impurity in the fuel to form Na_2SO_4 within the engine.

Despite considerable progress a sufficient understanding of the mechanistic details to provide predictive capability of hot corrosion within gas turbines does not

yet exist (ref. 4). This lack of understanding results primarily from limited knowledge of (1) the chemistry of the impurity elements in the combustion process; (2) the mode of deposition of the corrosive deposits (refs. 5 to 9); and (3) the interaction of these deposits, the surrounding vapors, and erosive particles with component materials (refs. 6 to 14). The complexity of the hot corrosion processes is indicated by noting that the lives of identical materials in the hot sections of nominally identical gas turbines can differ depending on engine application (ref. 15), quality of the fuel (ref. 16), engine maintenance procedures (ref. 17), and mission profile (refs. 18 and 19).

To further complicate matters, there is disagreement as to the applicability of laboratory testing procedures. Some researchers believe only engine tests or at least turbine simulators (where all or most major engine parameters are duplicated) can provide reliable information concerning component behavior (refs. 20 and 21). Unfortunately the nearer a test rig resembles an engine, the more prohibitive is the cost of building and running the simulator, the more difficult is the control and measurement of test conditions, and the more limited is the range available for each test parameter. Thus collecting each data point becomes costly, time consuming, and accompanied by a large uncertainty. Engine testing not only possesses all of these deficiencies, but findings in one type of engine are not necessarily applicable to another type of engine (refs. 22 and 23).

An approach to minimizing engine testing in the development of improved corrosion-resistant alloys and coatings has been to empirically correlate material response between a laboratory testing procedure and a specific turbine engine (e.g., refs. 15 and 24 to 31). The testing procedure often includes the screening of specimens of prospective materials in various types of burner rigs ranging in complexity from low to high gas velocities and atmospheric to higher pressures. Impurities associated with hot corrosion are introduced into the rig by the combustion air or the fuel or both. The responses of the materials in the rig are then used to predict their engine behavior on the basis of some preestablished empirical correlations. The ranking of alloys in the laboratory without benefit of a correlation to an actual engine, however, can be misleading. This is illustrated by the results of "round-robin" programs, where differences were reported in the corrosion resistance ranking of a set of superalloys by different laboratories (refs. 4, 32, and 33). Although the empirical approach has proven to be useful, it is limited to a particular type of engine for a particular application and, in some cases, is limited to a small range of alloys. Furthermore this approach does not contribute to a basic understanding of the corrosion process.

An approach often taken to provide basic understanding has been to model a single aspect of the

corrosion process at a time (i.e., investigate just that aspect in a controlled laboratory environment). Examples of this type of investigation include the thermogravimetric oxidation of salt-coated specimens to study the oxide scale fluxing process; the oxidation of presulfidized specimens (or specimens first exposed in an O_2 - SO_2 mixture) to study the sulfidation part of the process; impinging high-velocity particles on specimens in the combustion gases of a salt-seeded burner rig to study the erosion-corrosion interaction; and other such procedures (refs. 1, 3, and 34). Of course, the applicability of the results from these types of investigations depends on the correctness of the modeling, which is often judged by how closely the experiment can duplicate a certain morphology observed in corroded service parts. A problem of interpretation arises when the same morphology can be reproduced by two entirely different laboratory procedures. An example of this dilemma occurred in the laboratory testing for "low temperature" hot corrosion (ref. 35).

The present study is a continuation of an investigation into the deposition mechanism aspect of the hot corrosion process. In an earlier paper (ref. 36) the combustion gases of a Mach 0.3 burner rig were seeded with various salts ($NaCl$, Na_2SO_4 , and synthetic sea salt), and the deposition rate and deposit composition were determined as a function of the inert collector temperature. To interpret the results of this work, Rosner and his coworkers, under the sponsorship of NASA, developed the multicomponent chemically frozen boundary layer (CFBL) theory of salt deposition rates from combustion gases (refs. 36 to 41).

When the CFBL theory was applied to the Na_2SO_4 -seeded burner rig data, reasonably good agreement was found at temperatures far below the dewpoint. However, the theory predicted higher rates than observed just below the dewpoint even though the experimental dewpoints themselves compared favorably with the thermodynamically predicted values for all three salt compositions (ref. 36). The considerable scatter in the data of reference 36 suggested a need for better control of the burner rig test parameters in order to better define the comparison of experiment and theory. In addition, in this first program, 6 hours were required to collect each data point, and the lowest achievable collector temperature was restricted by the limited temperature range of the burner's combustion gases. Two distinct approaches have been undertaken to provide better experimental data. Rosner and his group built a flat-flame, low-velocity gas burner whose salt-seeded gases impinged upon a platinum ribbon (ref. 42). An electric current through the ribbon allowed it to be heated above the dewpoint temperature produced in the seeded combustion gases themselves. Upon reducing the heating current the dewpoint and deposition rates were measured on-line by

various laser-based optical means. This technique permitted the accumulation of numerous data in a short time. However, until now no provisions had been made to cool the ribbon collector below the temperature provided by the hot gases, thereby limiting the lower temperature range of the collector.

The second approach to collecting better experimental data is the subject of this paper. The purpose of this effort was to modify the Mach 0.3 burner rig and testing procedures in such a way as to reduce the scatter of the data, increase the temperature range of the collector, and decrease the time required to determine each data point. The chronological order of approach toward these objectives was as follows: Additional instrumentation was provided to improve the control of the burner rig. The collector was redesigned to be internally air cooled, allowing the collector temperature to be varied from over $1050^\circ C$ down to $500^\circ C$ at a constant combustion gas temperature. The salt solution concentration was increased to reduce the time required to accumulate measurable deposits. Then to further improve the data, a factorially designed experimental program was implemented to determine the remaining sources of variability in the data. This investigation in turn led to further rig modifications, a change in burner liner design, and the preheating of the combustion air.

Upon completion of these rig modifications and testing procedures, deposition rates and dewpoints were determined from burner rig runs in which the combustion gases were seeded with Na_2SO_4 , synthetic sea salt, K_2SO_4 , $NaCl$, and $NaNO_3$. These improved experimental data were compared with values calculated by using the CFBL theory. Supplementary tests were conducted to aid in interpreting the data and also to experimentally determine a value for the mass transfer Nusselt number, which would include the effect of free-stream turbulence.

Preliminary Considerations, Procedures, and Results

To appreciate the need for alterations in the burner rig design and testing procedures used in the present work, a brief description of the previous rig configuration, testing procedures, and results is required. The modifications to improve the rig and test designs are then outlined, and the results of preliminary experiments to assess the effectiveness of the changes are described and evaluated.

Original Experimental Procedures and Limitations

The type of burner rig used in the previous deposition testing has been described elsewhere (refs. 36 and 43) and is shown in figure 1, along with the collector assembly. The burner consisted of a housing and liner within which

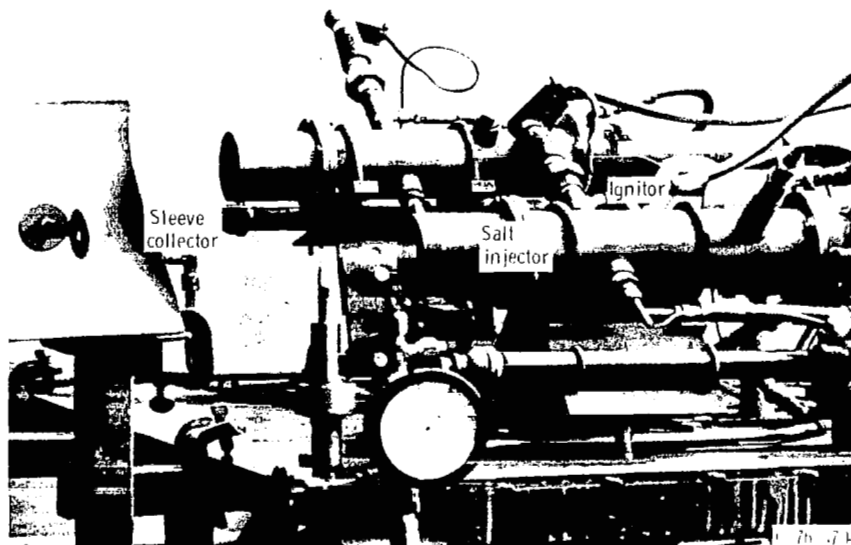


Figure 1. — Burner rig deposition testing configuration with sleeve-type collector.

jet fuel (ASTM D-1655) and air were mixed and ignited. The combustion products exited through an L605 (cobalt-base superalloy) nozzle onto a small Pt-10%Rh thin-walled sleeve collector backed by an Inconel support (fig. 2). The support contained a Chromel-Alumel thermocouple peened into a hole in its wall for monitoring the temperature of the collector. The entire assembly was rotated at about 100 rpm. The temperature of the collector was varied by varying the fuel-to-air ratio to alter the gas temperature of the burner. The range of fuel-to-air ratios allowing steady burner operation was limited, and with the configuration and distances shown in figure 1 this translated into collector temperatures ranging from 800° to 1030° C. The fuel flow and airflow

were measured with calibrated rotameters. The burner was controlled by a closed-loop system where the output of a visible radiation pyrometer focused on the collector was fed to a controller that operated an electric-to-pneumatic transducer. This transducer, in turn, adjusted the fuel flow valve in response to variations in the pyrometer signal in order to maintain a set-point temperature. The combustion airflow valve was manually set to provide a gage pressure of 6.9 kPa (1 psi) within the burner, thereby assuring Mach 0.3 operation.

The salt solution, either NaCl, Na₂SO₄, or synthetic sea salt (ASTM D-1141-52, table I), was pumped into the combustor by a peristaltic pump at a calibrated flow rate of 200 milliliters/hr. The solution was air atomized into a fine spray within the combustion chamber downstream of the ignitor (fig. 1). The concentration of the salt solutions were based on collecting measurable deposits in the 6-hour run time. Higher salt concentrations would have permitted shorter run times, but access to the test cell was limited to once a day because the other three burners located in the same cell were involved in endurance tests. After each run the salt deposited on the collector was weighed and chemically analyzed.

An example of the data obtained (ref. 36) is shown in figure 3, along with the theoretical curve. The theoretical curve was generated from the CFBL theory of Rosner and coworkers (refs. 36 to 42). Reasonably good agreement was found at temperatures far below the dewpoint, but the theory overpredicted observed rates just below the dewpoint. The dewpoint temperatures themselves compared favorably with the thermo-

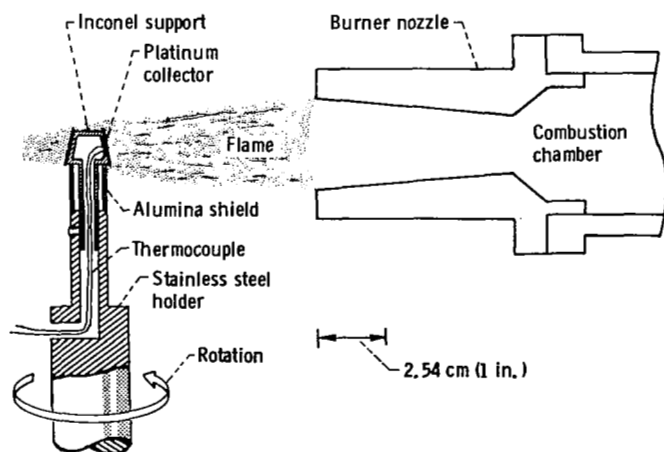


Figure 2. — Schematic of collector sleeve and support assembly.

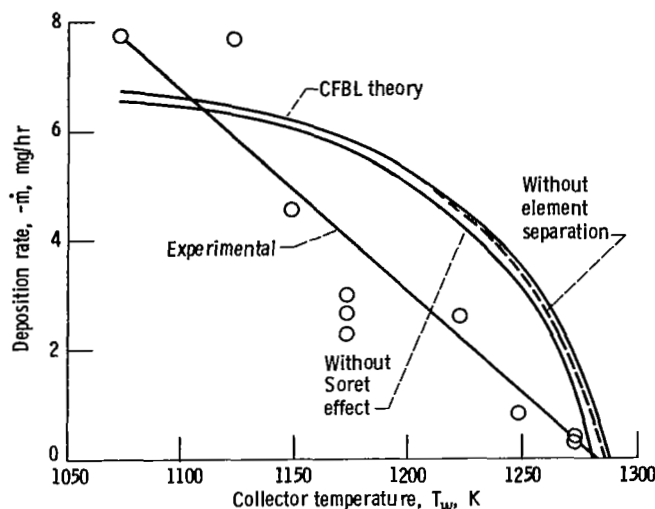


Figure 3. — Effect of collector temperature predicted and experimental Na_2SO_4 deposition rates for sleeve type of collector configuration. Ambient pressure, 1 atm.

dynamically predicted values. Also, considerable scatter is evident in the experimental data.

Briefly, Rosner's theory predicts a deposition flux resulting from simultaneous Fick (concentration) diffusion, Soret (thermal) diffusion, convection, and turbulence through a gaseous boundary layer between the combustion gases and the surface of the collector. Thermodynamic equilibrium is assumed to exist at the outer and inner edges of the boundary layer. The boundary layer is assumed to be chemically frozen or "source free." This means that no chemical reaction, condensation, nucleation, or coagulation occurs within this layer. All of the sodium added to the combustion gases is available for transport to the collector via vapor species (e.g., NaCl(g) , NaOH(g) , Na(g) , and $\text{Na}_2\text{SO}_4\text{(g)}$). The mass flux for each such species i at the surface is given by

$$-j''_{i,w} = \left[F_{\text{turb}} \frac{(D_i \rho)_{\infty}}{L} F_{i,\text{Soret}} \text{Nu}_{m,i} \right] \times \left[(\omega_{i,\infty} - \omega_{i,w}) - B_{T,i} \frac{F_{\text{ncp}}}{F_{i,\text{Soret}}} \omega_{i,w} \right] \quad (1)$$

where all symbols are defined in appendix A.

In the absence of main-stream turbulence, thermal diffusion, and variable property effects, equation (1) reduces to the familiar form

$$-j''_{i,w} = \frac{(D_i \rho)_{\infty}}{L} \text{Nu}_{m,i} (\omega_{i,\infty} - \omega_{i,w}) \quad (1a)$$

For details of the CFBL theory see references 38 and 39 and the recently compiled CFBL computer manual (ref. 44).

Burner Rig and Experimental Modifications

A new Mach 0.3 burner rig was built to provide better experimental data to compare with the CFBL deposition theory (less scatter and an expanded collector temperature range) and to provide for more efficient data collection. This rig is similar to the one just described, but with added instrumentation and located in a separate cell with unlimited access. Also, the collector assembly was redesigned to provide for internal air cooling and a more amenable geometry for ease of calculating transport parameters across the boundary layer (figs. 4 and 5). The collector itself was a Pt-20% Rh cylinder, 1.9-cm (3/4-in.) o.d. by 1.3 cm (1/2 in.) high with a 0.6-cm (1/4-in.) deep vertical hole in its 0.3-cm (1/8-in.) thick wall for accepting a Pt/Pt-13% Rh thermocouple. Above and below the collector were 1.9-cm (3/4-in.) o.d. by 3.8-cm (1.5-in.) long ceramic tubes (spacers). The lower spacer contained a longitudinal groove to accommodate the ceramic-sheathed thermocouple leads. Within the cylinder formed by the collector and its ceramic spacers was an Inconel tube, closed at the top and perforated with small holes. The collector was cooled from within by the impingement of air from these holes. The collector and spacers were spring loaded to allow for thermal expansion and to assure intimate contact of the enclosed thermocouple head with the collector.

Preliminary tests were conducted to verify that the temperature readings from the embedded thermocouple were the same as those on the surface when the collector was internally cooled. This was accomplished by simultaneously comparing the output of the embedded thermocouple with that of a thermocouple whose bead was peened into a hole through the surface of the collector (fig. 6). The small dimensions of the collector, along with its rotation in the combustion gases (about 200 rpm), assured a uniform temperature over its entire surface, as was verified by using an optical pyrometer.

This collector assembly design allowed deposition runs to be conducted at constant flame temperatures (constant fuel-to-air ratios) while the collector temperature was varied over a large range. For example, with the collector rotating in combustion gases with temperatures as high as 1600° C, the temperature of the collector could be varied from over 1050° C down to 500° C.

To cover this large temperature range, two different ceramic materials were required for the spacers in the collector assembly. At low collector temperatures, below 850° C, spacers made of Si_3N_4 were used because of their good thermal shock resistance. Above 850° C, however, the Na_2SO_4 deposit reacted with the Si_3N_4 to form vitreous silica, which caused the spacer to stick to the collector and the sheath of the thermocouple leads. Thus above 850° C less reactive Al_2O_3 spacers were used, thermal shock being much less severe than at the lower temperatures when more cooling air was required.

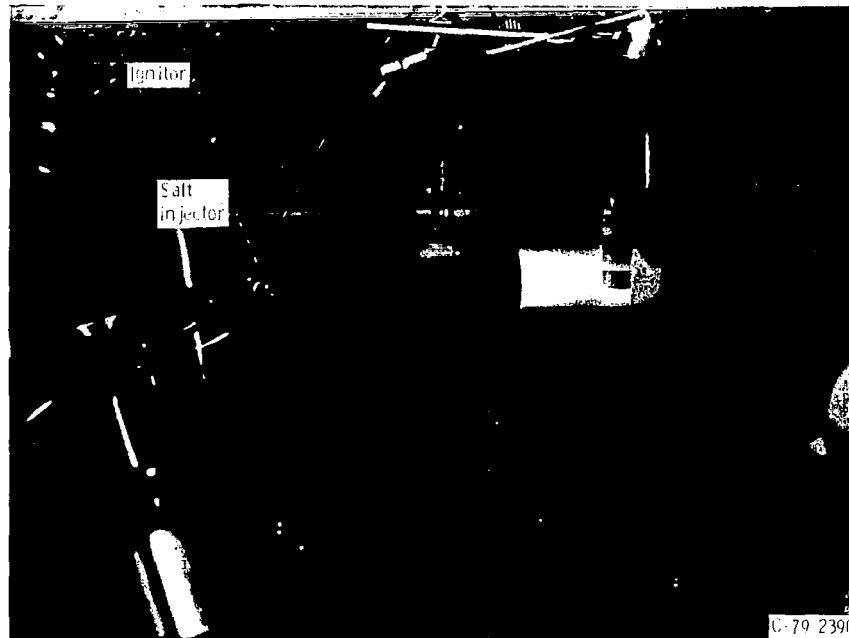


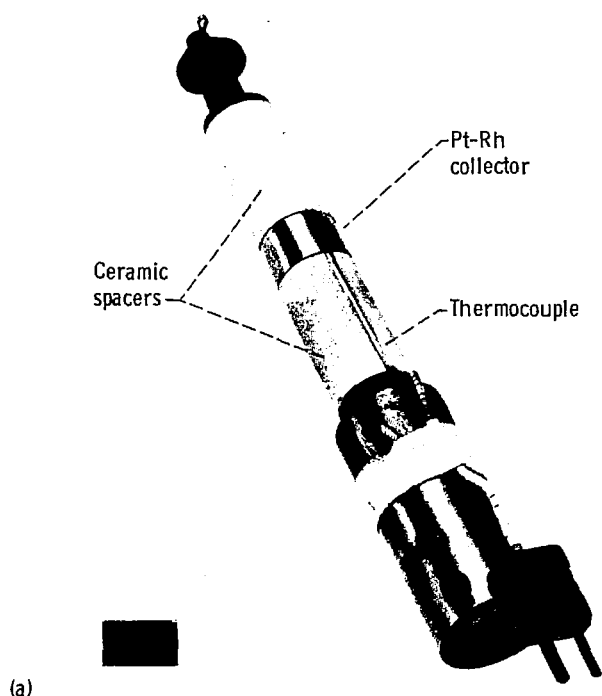
Figure 4. - Burner rig deposition configuration with internally cooled collector.

The enclosed thermocouple in the collector not only measured the temperature of the collector, but was also used as a signal source to operate a closed-loop cooling air control system. The signal from the thermocouple was fed to a controller that operated an electric-to-pneumatic transducer. This transducer adjusted the cooling airflow valve in response to deviations from the set point of the controller as sensed by the thermocouple. The fuel flow was controlled by a similar closed-loop system. A Pt/Pt-13% Rh thermocouple located downstream of the collector provided the necessary signal for the fuel control system. The combustion airflow valve was set manually to provide a gage pressure of 6.9 kPa (1 psi) within the burner. The combustion airflow and fuel flow were measured by calibrated turbine flowmeters. The maximum flows were 2.1 milliliters/sec (2 gal/hr) of fuel and 37.8 g/sec (300 lb/hr) of air. To obtain the large range of collector temperatures at constant flame temperatures, the cooling air gage pressure was varied from near zero to about 4.1×10^5 Pa (60 psi). A simplified schematic of the flow systems and controls is given in figure 7.

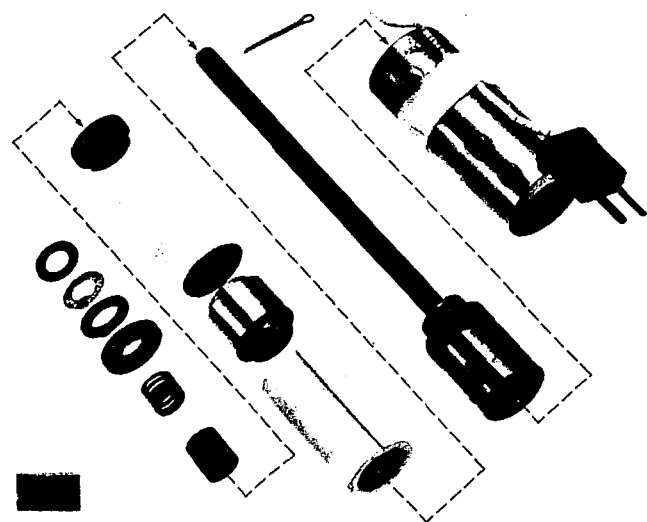
A few preliminary tests were conducted to see if collector distance from the exit nozzle affected deposition rate, all other parameters except cooling airflow being the same. The distance between the collector and the exit nozzle could be readily varied from <1.27 to >30.5 cm ($<1/2$ to >12 in.). This provision of the burner was accomplished by mounting the entire rotating shaft assembly on a plate on the front of the burner stand. The

plate could be drawn from the stand on four horizontal cylindrical supports (fig. 8). Flexible electrical and cooling air connections were made to the component parts on the shaft assembly. This assembly consisted of the collector assembly, a hollow shaft, a thermocouple connector, a thermocouple slip ring (allows temperature measurements to be made on a rotating system), and an electric motor with belt connection to a centrifugal switch. The role of the centrifugal switch was to shut down the burner if rotation ceased because of, for example, binding of the shaft. Changes in the distance between the exit nozzle and the collector did not result in a detectable change in the amount of deposit.

The adjustability of the collector-to-exit-nozzle distance allowed the ready substitution of exit nozzles of different sizes. The long exit nozzle shown in figure 4 was used in the preliminary tests, but the bulk of the testing was conducted using a short exit nozzle made of RA 330 (Fe-35Ni-19Cr-1.25Si-1.5Mn-0.5C) with the leading surface of the collector at about 1.3 cm (1/2 in.) from the nozzle. The purpose here was to have the collector within the isentropic zone of the flame (fig. 8(a)). With this burner configuration about half as much mass flow was required for the same collector temperature as was needed with the configuration of the first program (fig. 1). However, the trim on the fuel flow valve was not properly sized to accommodate this reduction in mass flow. To maintain the versatility of the rig, the valve trim was not altered, but a fuel bypass line was installed upstream of the fuel flowmeter (fig. 7(b)). Thus either



(a)



(b)

(a) Assembled.
(b) Exploded view.

Figure 5. — Internally cooled collector.

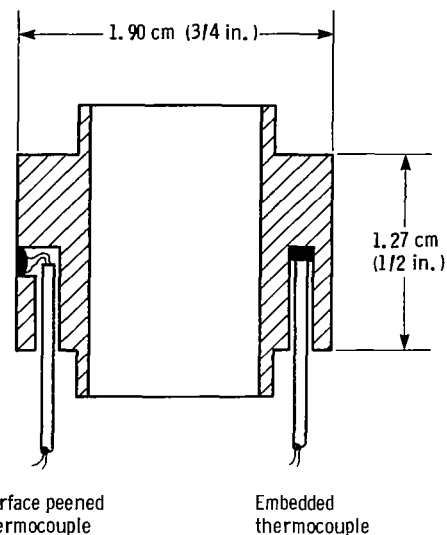


Figure 6. — Specially thermocoupled internally cooled collector used to verify surface temperature.

long (and massive) or short burner exit nozzles could be used merely by adjusting the bypass valve in the fuel return line.

Another feature of this revised system was the installation of a probe actuator that permitted the remote positioning of flame probes. Figure 9 shows the actuator and the position of a sonic temperature probe when sensing combustion gas temperature and its position when the burner is arced into the collector heat position. Details of the use of this feature will be given when describing the experiments in which the actuator and probes were employed.

In the previous program the salt solution flow was set by the speed of the peristaltic pump and the amount actually consumed was determined by the weight change in the solution reservoir before and after each run. In the modified system, the flow rate was set as before but the amount consumed was continuously monitored either by the weight change of the reservoir as sensed by a load cell, or by the volume change where the reservoir was a graduated cylinder that could be viewed from the observation window of the test cell.

Preliminary Tests and Results

Some of the preliminary testing to verify the adequacy of the rig has been referred to in describing the rig modifications. In addition to these, preliminary tests were also conducted to determine the effect of the following parameters on deposition: time, collector temperature, salt flow rate, salt solution concentration, salt injector geometry and orientation, and collector rotation speed. As in the previous program, the sulfur content of the Jet A-1 fuel varied from 0.02 to 0.06 wt %. The sulfur in the fuel was analyzed each time the fuel

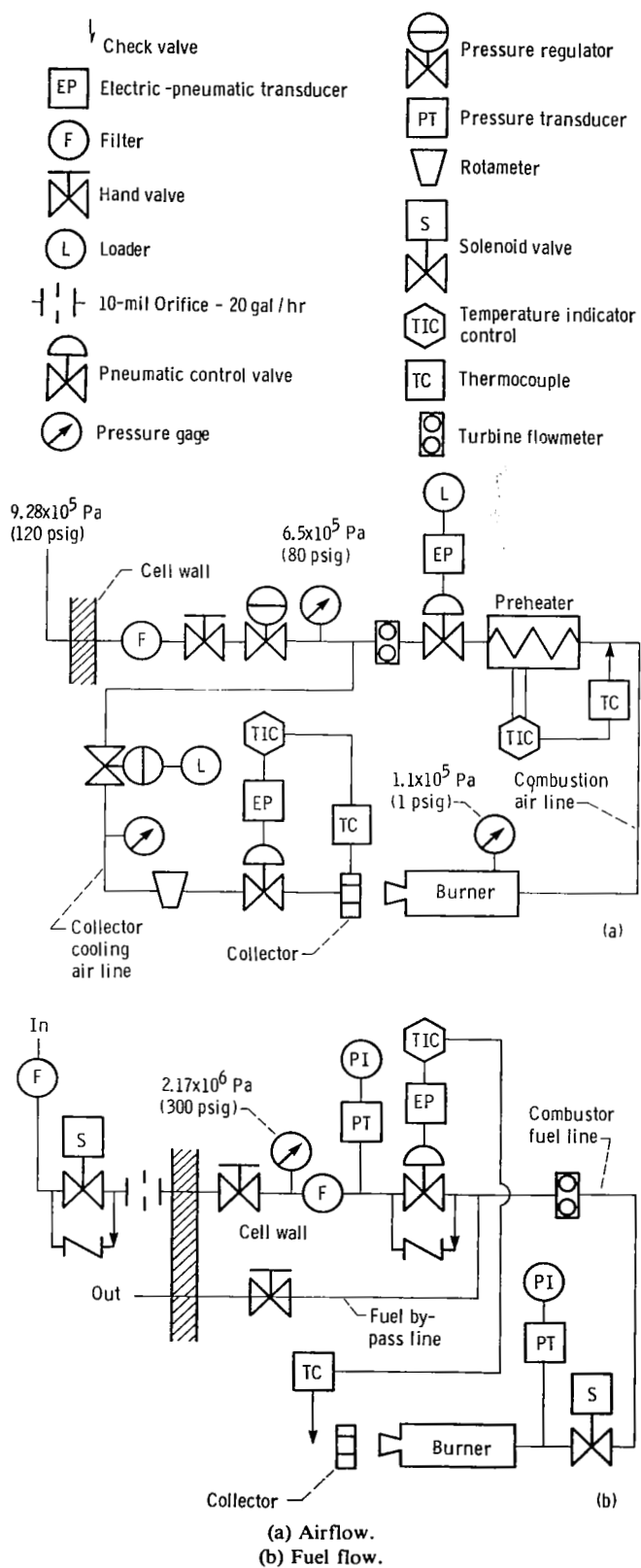
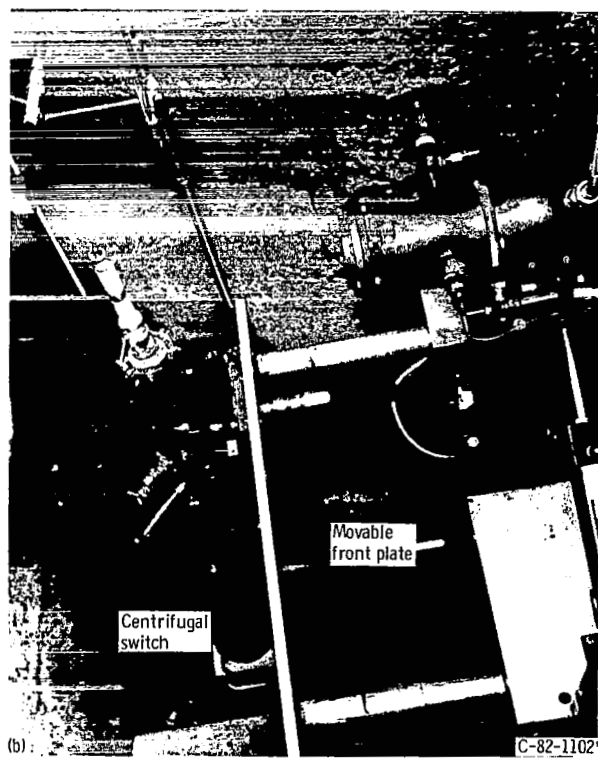
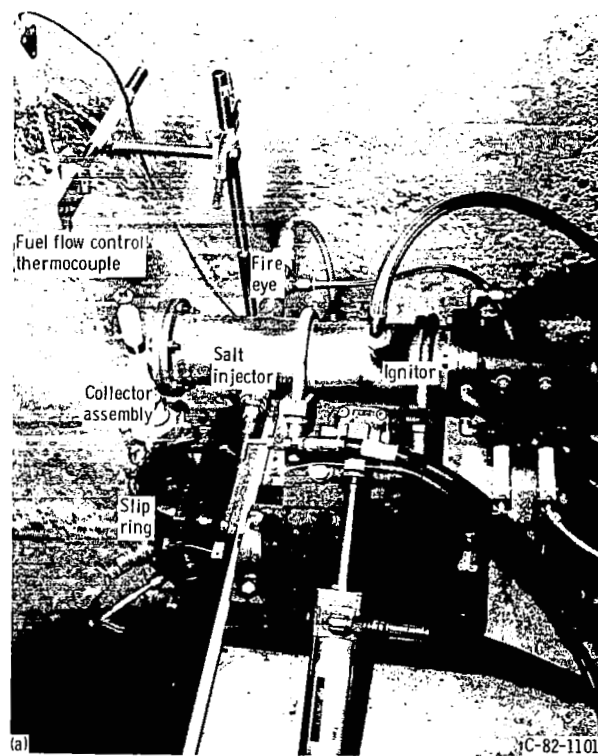
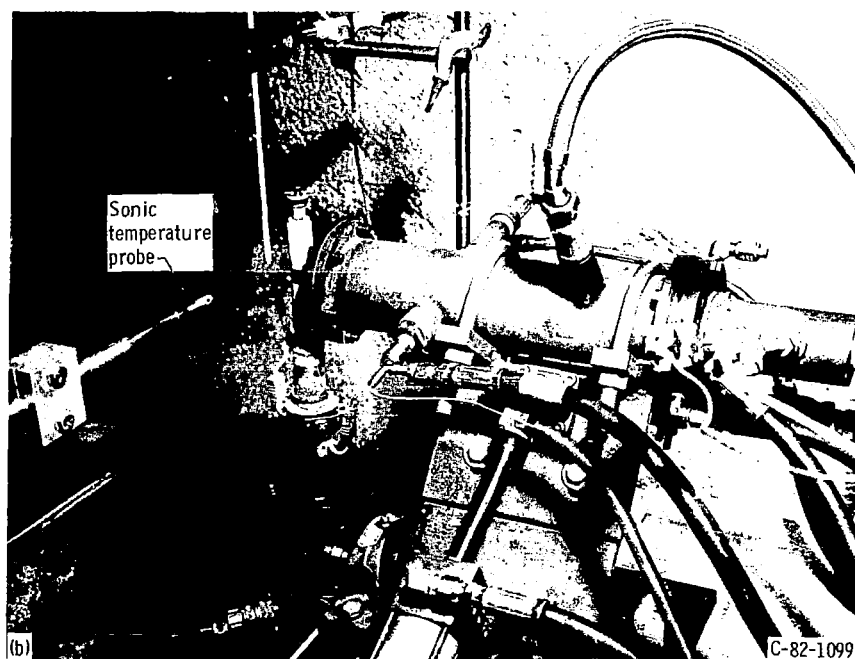
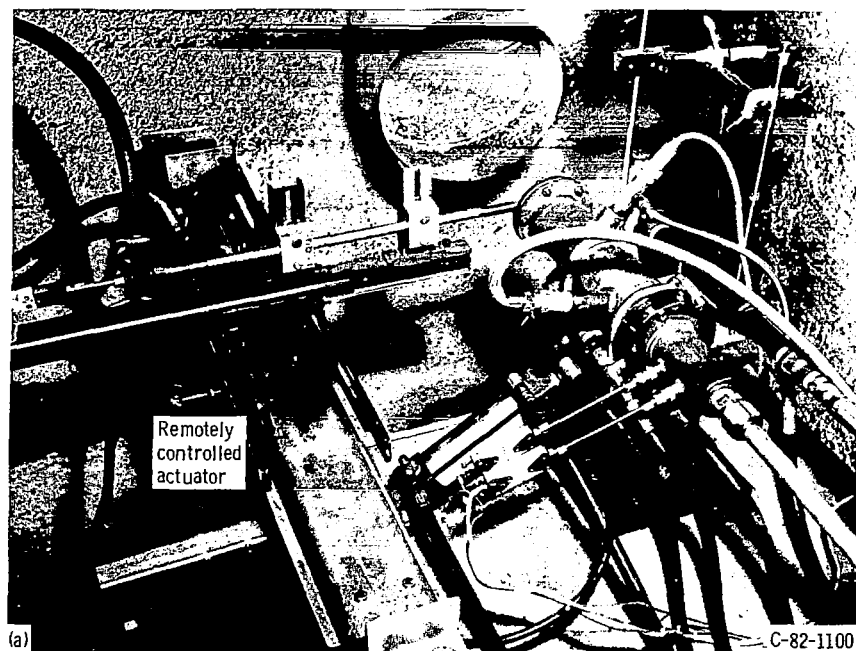


Figure 7. - Schematic representation of flow systems and controls.



(a) Closed.
 (b) Extended.

Figure 8. - Position of burner stand front plate with rotating shaft assembly.



(a) Probe position for sensing combustion gas.
 (b) Probe position when burner is in the collector heat position.

Figure 9. – Remotely controlled probe actuator with sonic temperature probe.

tank was refilled. Solutions of Na_2SO_4 were used in all of these tests. The amount of salt deposited was measured by weighing the amount accumulated on the collector during the run and the amount scrubbed off the collector after the run. These two weights were usually within 0.2 mg of each other (i.e., within the precision of the analytical balance).

The data in figure 10 indicate that the deposition rate was linear with time within the time frames shown, with the exception of the 900°C data. Figure 11 represents the rate of deposition for various collector temperatures at a constant combustion gas temperature. Each data point represents a 30-minute run. The main feature of the data is the sharp peak at about 850°C (close to the 884°C

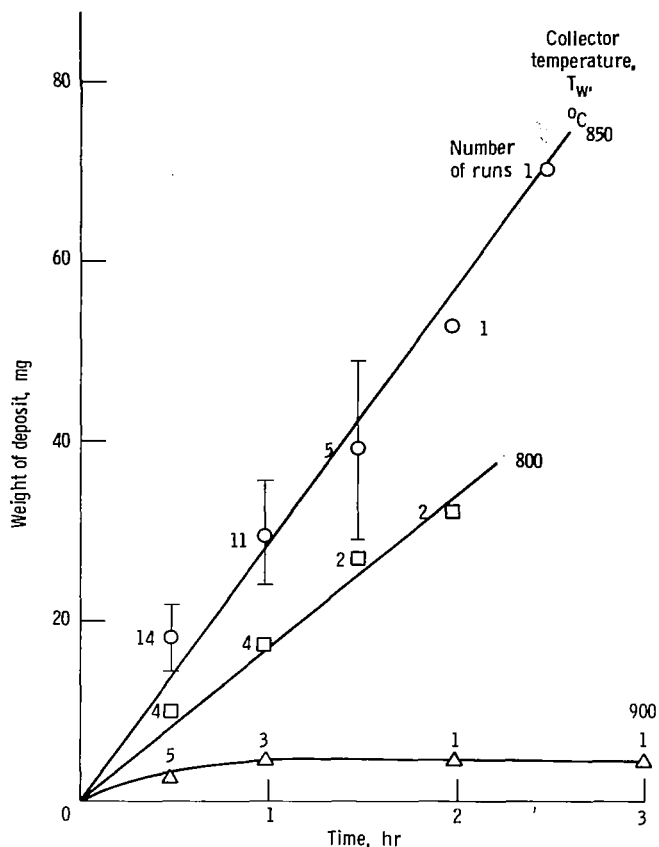


Figure 10. - Rate of deposition of Na_2SO_4 -seeded runs at collector temperatures indicated. The larger scatter of the data at 850°C reflects the mixing of data from runs with four different burner liners.

melting point of Na_2SO_4) with steep declines at temperatures to either side of the peak. CFBL theory predicts a plateau (nearly constant deposition rate) at lower collector temperatures with a fast rise from the dewpoint temperature to this plateau level. By assuming a plateau value (in this case the peak deposition rate) and using a calculated dewpoint based on thermodynamics only, a representation of the theoretical curve (its shape but not its magnitude) can be expressed by equation (2)(ref. 42):

$$\frac{-\dot{m}''(T_w)}{-\dot{m}''(0)} = 1 - \exp \left[\frac{-\Lambda}{RT_{dp}} \left(\frac{T_{dp}}{T_w} - 1 \right) \right] \quad (2)$$

Equation (2) results from dilute vapor diffusion theory for a single, nondissociated vapor whose condensation rate is simply proportional to the difference between its partial pressure prevailing in the combustion gases and its equilibrium vapor pressure over the condensate. The derivation is given in appendix B. Equation (2) provides a quick comparison of the data with the shape of the theoretical curve, ignoring the magnitude of the data.

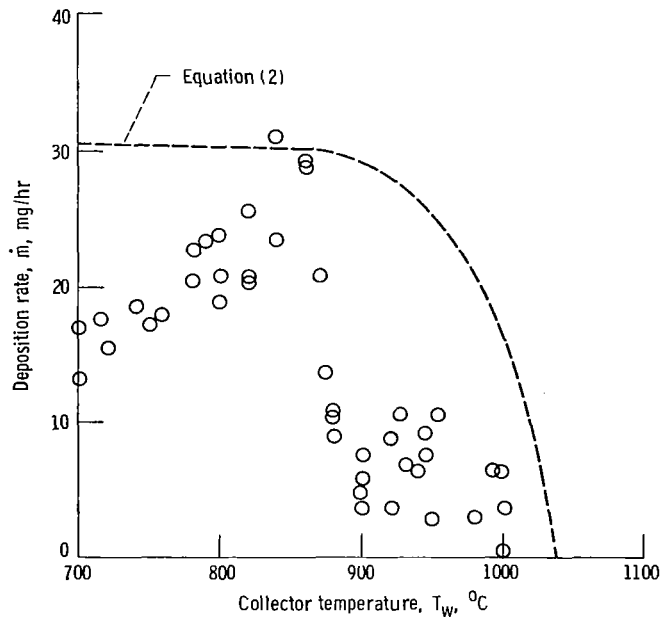


Figure 11. - Deposition rates from Na_2SO_4 -seeded burner at constant combustion gas temperature. Run duration, 30 min; sodium concentration, 6 ppm with respect to combustion air mass. (The data were accumulated from runs with three different burner liners.)

The theoretical magnitude of the rate at each temperature can be calculated, of course, by using equation (1), but for now the purpose is just to compare the shape of the experimental curve with that of the predicted curve. Later in the report the results of studies that address the disparity between theory and experiment are discussed in detail.

The effect of varying the salt solution pump speed (salt solution flow rate into the combustor) is presented in figure 12 for two concentrations of Na_2SO_4 solution. The nominal salt solution flow rate used throughout this program was 200 milliliters/hr, unless otherwise stated, as in the case here. The data indicate a direct proportionality between the amount of deposit on the collector and the quantity of salt entering the combustor. Figure 13 represents the effect of salt solution concentration on the deposition rate. At high salt concentrations and with long run times, the constant amount of deposit observed was speculated to be a result of newly introduced mechanisms. This phenomenon was attributed to the prevailing balance between the mass arrival and departure rates due to events such as entrainment and spalling. Apparently there is a limit to the amount of deposit than can adhere to the collector. With more concentrated solutions and lower air mass flow rates through the combustor (both contributing to an increased salt concentration in the combustion gases) and with longer collector exposure times, this limit had been exceeded.

The orientation of the salt solution injector as it affects the deposition rate was studied. Four configurations were

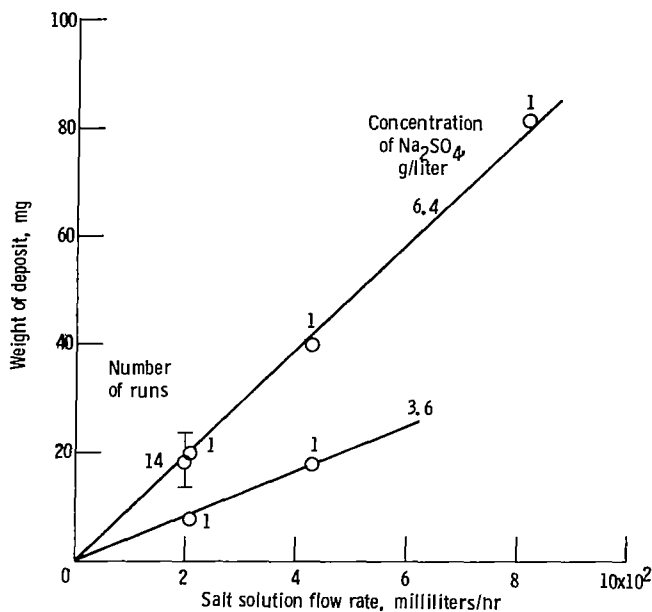


Figure 12. - Effect of Na_2SO_4 solution flow rate on deposition rate for two salt solution concentrations. Run duration, 30 min; collector temperature, 950°C ; combustion air mass flow rate, $109 \pm 4 \text{ kg/hr}$ ($240 \pm 9 \text{ lb/hr}$).

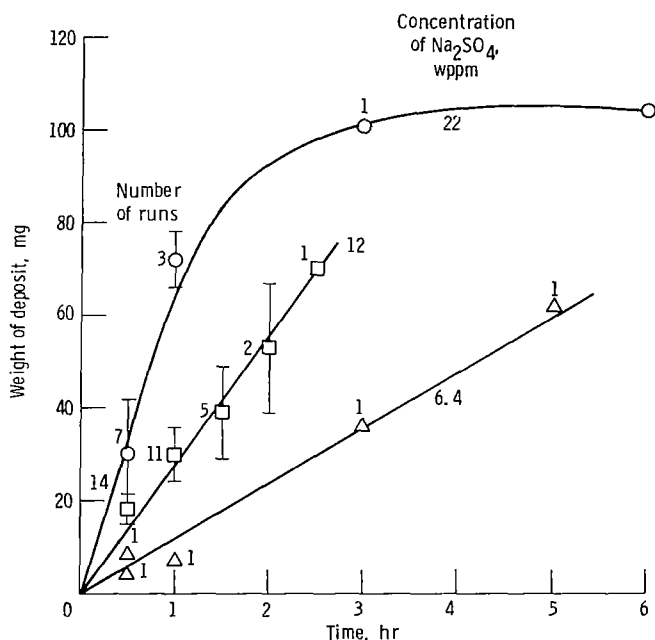


Figure 13. - Effect of Na_2SO_4 solution concentration on deposition rate. Collector temperature, 850°C ; solution flow rate, 200 milliliters/hr. Salt concentrations are given with respect to the combustion air mass.

considered. The standard configuration used in all the Mach 0.3 burner rigs at Lewis has a 0.64-cm (1/4-in.) o.d. injector inserted into the combustion gases at about 10.8 cm (4.25 in.) from the throat of the exit nozzle. The probe penetrates one-quarter of the diameter of the

combustor liner and faces downstream, discharging a fine mist of droplets at a 20° angle (fig. 14). The salt solution is pumped through an inner tube of the probe and is atomized by pressurized air flowing through an outer concentric tube. The atomizing air is at a gage pressure of 34 kPa (5 psi). The other orientations are also shown schematically in figure 14: the standard injector penetration but facing upstream, and a 1/2-liner-diameter depth of penetration with the salt injector facing either upstream or downstream. The average deposition rates are given for each of the four configurations. No variation of the values were observed beyond the scatter in the data. However, this scatter was greater than anticipated. Thus these results are inconclusive.

Another experimental parameter that was investigated was collector rotation speed. Figure 15 indicates no effect on deposition rate with rotation speeds from zero to over 1700 rpm. The standard speed used throughout these studies was 230 rpm.

These preliminary test results indicated that the modified burner rig functioned well, but the scatter in the amount of deposit was about the same as in the previous program and the shape of the deposition rate curve did not agree with the CFBL theory. Apparently other parameters are involved or some of the assumptions used in the theory are not applicable for this situation.

Factorial Design Procedures and Results

To ascertain the extent to which other factors are involved in the experimental method used herein to study deposition, a factorial design approach was used to consider quantitatively the influence of these parameters on deposition rate. The program was designed by Steven M. Sidik of NASA Lewis and only the results are discussed herein. The parameters investigated were (1) collector temperature, (2) Na_2SO_4 solution flow rate, (3) time trends, (4) collector-to-collector variation, (5) burner-liner-to-burner-liner variation, and (6) combustion gas temperature. Parameters (1) and (2) had already been studied but were included for completeness. The idea was to conduct the program in such a way as to minimize the number of experimental runs and at the same time to be able to separate the influence of each of the parameters on the deposition rate. Any significant variability not accounted for by these parameters would indicate the existence of a significant parameter or parameters not yet considered in the testing. The details of the experimental procedures are described next.

At the beginning of each day of testing, a new liner was placed in the combustor and a randomly chosen collector was installed. The burner was turned on and allowed to

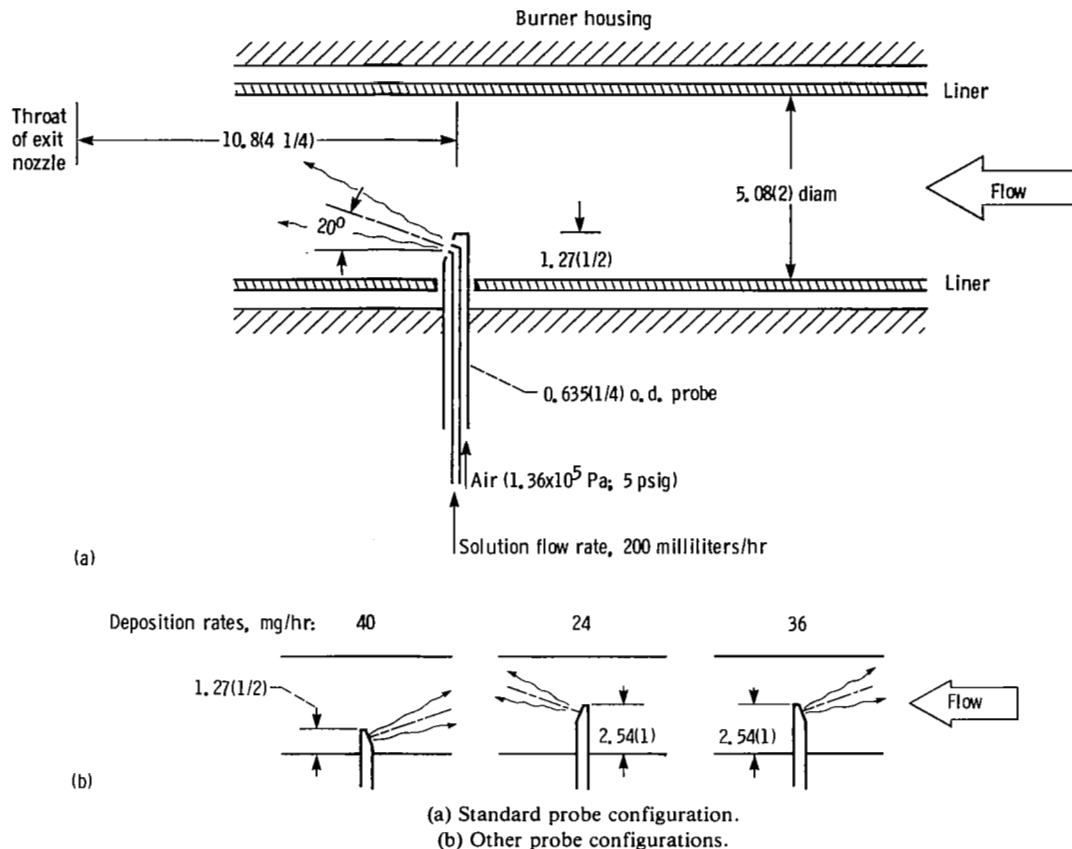


Figure 14. - Effect of salt solution probe orientation on deposition rate from a Na_2SO_4 -seeded burner. Run duration, 30 min; collector temperature, 850°C . (Dimensions are in centimeters (inches).)

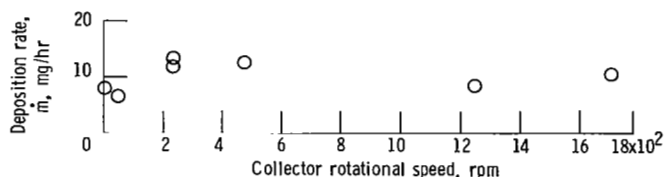


Figure 15. - Effect of collector rotational speed on deposition rate. Run duration, 30 min; collector temperature, 895°C ; salt concentration, 18-ppm Na_2SO_4 in combustion air.

warm up for 30 minutes, more than enough time to reach steady-state conditions. The desired fuel-to-air ratio was set, and the flame temperature was measured with a sonic probe that could be remotely located to any position in two planes within $\pm 2.5 \times 10^{-3}\text{ cm}$ ($\pm 0.001\text{ in.}$). In these tests the probe tip was located in the center of the throat of the exit nozzle, at the same distance from the throat as the forward surface of the collector would be located (i.e., 1 cm (0.4 in.), fig. 9). The burner was then moved into the heat position. Internal cooling airflow within the collector was adjusted to obtain the desired collector temperature. The salt pump was switched on. Thirty minutes later the burner was moved out of the heat

position and simultaneously the salt pump was switched off. The flame temperature was checked again. The collector was force cooled by increasing its internal cooling airflow. The amount of solution consumed was noted, the collector was removed, and a new collector was installed (all without turning off the burner to save heat-up time). Then a new run cycle would begin. Six such runs were made each day. The amount of salt deposited on the collectors was measured and then the collectors were cleaned and weighed in preparation for reuse.

The salt pump speed was calibrated for each change in salt solution flow rate by noting the time required to pump the solution into a graduated cylinder to a convenient volume and adjusting the pump speed accordingly. In selected runs the deposit was analyzed by using the scanning electron microscope (SEM), energy dispersive spectrography (EDS), and X-ray diffraction (XRD). The overall factorial design program was divided into two parts. Part 1 consisted of the flame and salt flow parameters both at their low or both at their high levels. Virgin burner liners were used in part 1. In part 2, when one of these two parameters was at its high level the other

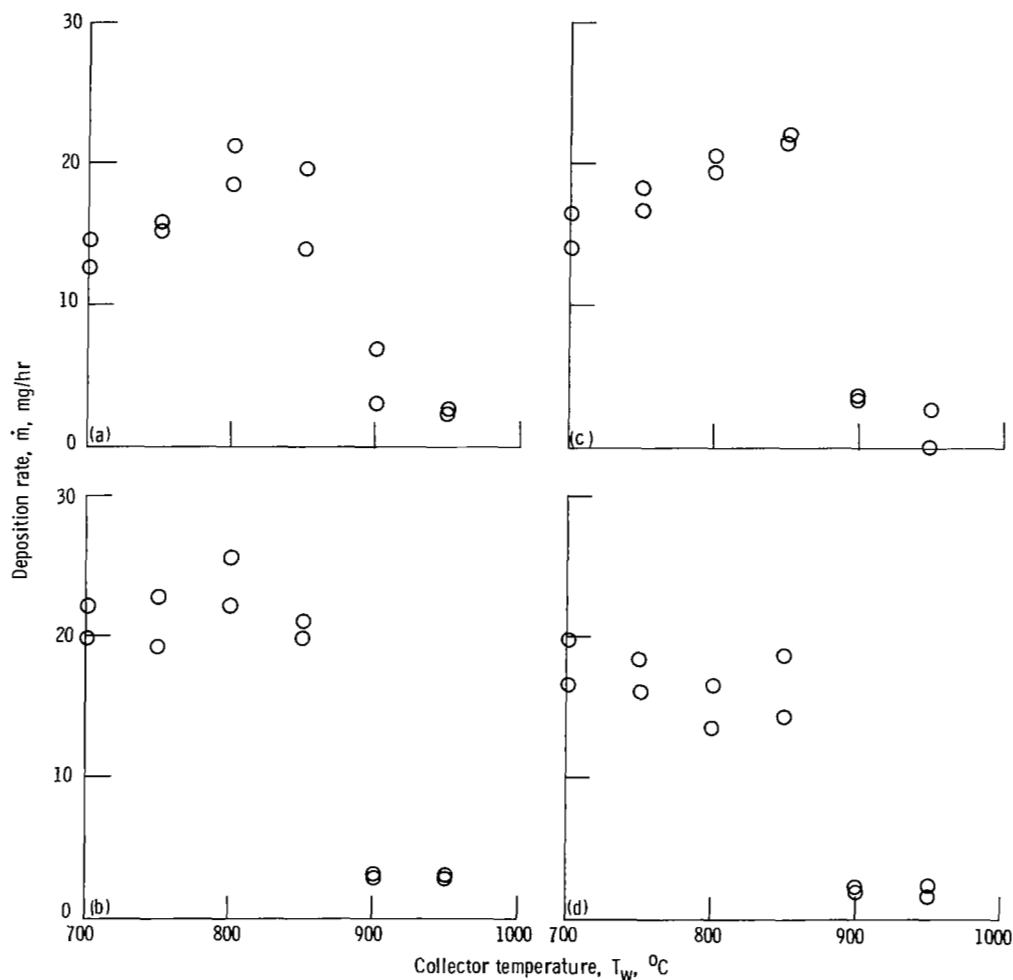
was at its low level. The burner liners used in part 1 were cleaned and reused in part 2.

Figure 16 represents the data from part 1 and figure 17, the data from part 2. There was a noticeable increase in scatter in part 2 over that in part 1, perhaps indicating some deterioration of the liners. In spite of the scatter in the data, two characteristics can be distinguished: (1) at the higher flame temperature, the curves tended to plateau at low collector temperatures as theory predicts; (2) liner variation caused a significant change in the magnitude of the curves.

X-ray diffraction patterns from deposits on collectors exposed at 750°, 800°, and 900° C to the high salt flow rates and high flame temperatures revealed only one phase, Na_2SO_4 (thenardite—form V, ASTM 5-631), along with a few very weak unidentified lines. However, the NASA complex chemical equilibrium computer (CEC) code (ref. 45), predicted deposits of Na_2CO_3 and

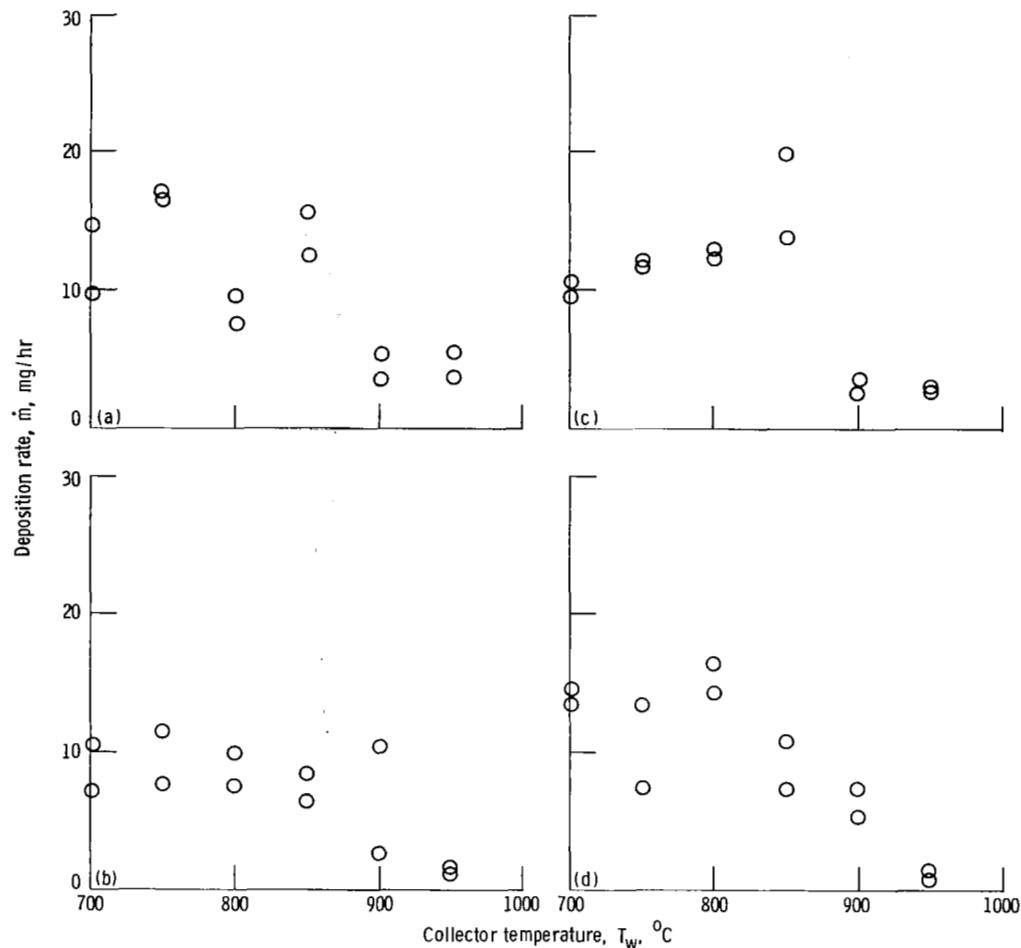
no condensed Na_2SO_4 for these conditions. The computer program indicated the dewpoint temperature for Na_2CO_3 to be 854° C.

Several possibilities can be offered to explain the discrepancy between the predicted and observed condensate phases. The Na_2SO_4 -to- Na_2CO_3 transition is quite sharp. A slight inaccuracy in the fuel-to-air ratio, and thus the gas composition, could give a misleading expectation of the stable condensed phase. Another possibility is that the vapor composition at the collector wall differed slightly from that thermodynamically predicted from the main-stream composition because of the different mobilities of the vapor species diffusing through the boundary layer (refs. 36 and 46). This transport effect on the composition at the wall side of the boundary layer may have been sufficient to shift the equilibrium of the condensate to Na_2SO_4 . The final possibility is that the deposition mode was not by vapor



- (a) Low combustion gas temperature and low salt solution flow rate with liner 1.
- (b) High combustion gas temperature and high salt solution flow rate with liner 2.
- (c) Low combustion gas temperature and low salt solution flow rate with liner 3.
- (d) High combustion gas temperature and high salt solution flow rate with liner 4.

Figure 16.—Effect of collector temperature on deposition rate—factorial design Na_2SO_4 -seeded burner rig experiment (part 1).



(a) Low combustion gas temperature and high salt solution flow rate with liner 1.
 (b) High combustion gas temperature and low salt solution flow rate with liner 3.
 (c) Low combustion gas temperature and high salt solution flow rate with liner 2.
 (d) High combustion gas temperature and low salt solution flow rate with liner 4.

Figure 17. — Effect of collector temperature on deposition rate—factorial design Na_2SO_4 -seeded burner rig experiment (part 2).

diffusion but by inertial impaction of incompletely evaporated Na_2SO_4 droplets. In such a case there may not have been sufficient time at the collector temperature for conversion of the Na_2SO_4 to the stable Na_2CO_3 phase.

A statistical analysis of the data by Sidik (personal communication) indicated that all significant parameters were considered in these experiments, the remaining variability (scatter) being “statistical noise.” The collector temperature and the Na_2SO_4 solution flow rate parameters behaved as in past experiments, except for the plateau in the deposition rate curve at high fuel-to-air ratios. There was a slight trend effect, variation in the data from any one liner with time, which is thought to be due to coking of the liner. The effect was more noticeable at high fuel-to-air ratios, which is consistent with the coking interpretation. The trend effect is not to be confused with the effect due to the deterioration that had

occurred when the liners were reused in part 2 of the program. The trend effect suggests the need to preheat the combustion air before mixing it with the fuel in the combustor. There was no significant variation in the deposition rates associated with the six different collectors used in the program, no collector-to-collector variation. As indicated in figures 16 and 17, a significant liner effect was detected. This effect is thought to be due to variation in the degree and configuration of warping of the open end (hot end) of the liner from one liner to another, suggesting the need to reinforce this section of the liner.

Principal Test Procedures and Results

The factorial design experiments clearly indicated the need to modify the burner liner to eliminate liner-to-liner

variation in the deposition rate. The less bothersome trend effect was thought to be caused by coke formation on the liner and thus to be a much easier problem to deal with. The rig was successfully modified and the principal testing accomplished as described here.

Additional Rig Modifications

Burner liner changes significantly influenced the rate of deposition. It is conceivable that the effect was caused by the warping of the hot end of the liner as suggested previously. The liner was attached to a swirl plate that was fixed to the burner housing, but the hot end was setting unattached on the combustor side of the exit nozzle, allowing the liner to expand when heated. To minimize the warping and still allow the liner freedom to expand, the liner was modified by adding a collar around the open end (fig. 18). The modification reinforced the exit end of the liner and insured a uniform flow of secondary air egressing into the gas stream near the throat of the exit nozzle. Some time after the liner modification was made, a combustor air preheater was added to the system that heated the air intended for combustion to about 260° C. The liner modification significantly reduced liner-to-liner variation and the preheated air reduced coking of the liner and therefore the trend effect. The liner modification, however, had an unexpected effect that is discussed next.

Principal Test Parameters

In the experiments described here, the common testing parameters were the short exit nozzle and the collar liners (fig. 18), an internally cooled Pt-20% Rh collector of 7.6-cm² (1.2-in.²) area located 1 cm (0.4 in.) from the exit nozzle, 30-minute runs, collector rotation at 230 rpm, and a salt solution flow rate into the combustor of about 200 milliliters/hr. These parameters became the standard for subsequent testing. The burner was individually seeded with the following salts: Na₂SO₄, synthetic sea salt, K₂SO₄, NaCl, and NaNO₃. The molar concentration of the alkali element for each salt with respect to the combustion air was about 8 ppm. The main difference in the procedures for these tests as compared with previous tests was the use of the collar liners. The Na₂SO₄ and the synthetic sea salt runs used the original collar liner. The remaining tests used several collar liners. The second set of data from K₂SO₄-seeded runs and the NaCl and NaNO₃ tests employed preheated combustion air in addition to several collar liners.

Na₂SO₄ Results

The data for Na₂SO₄ are shown in figure 19. The surprising feature of these data is that even at the relatively low fuel-to-air ratio used, the deposition rate was fairly constant at low collector temperatures. This

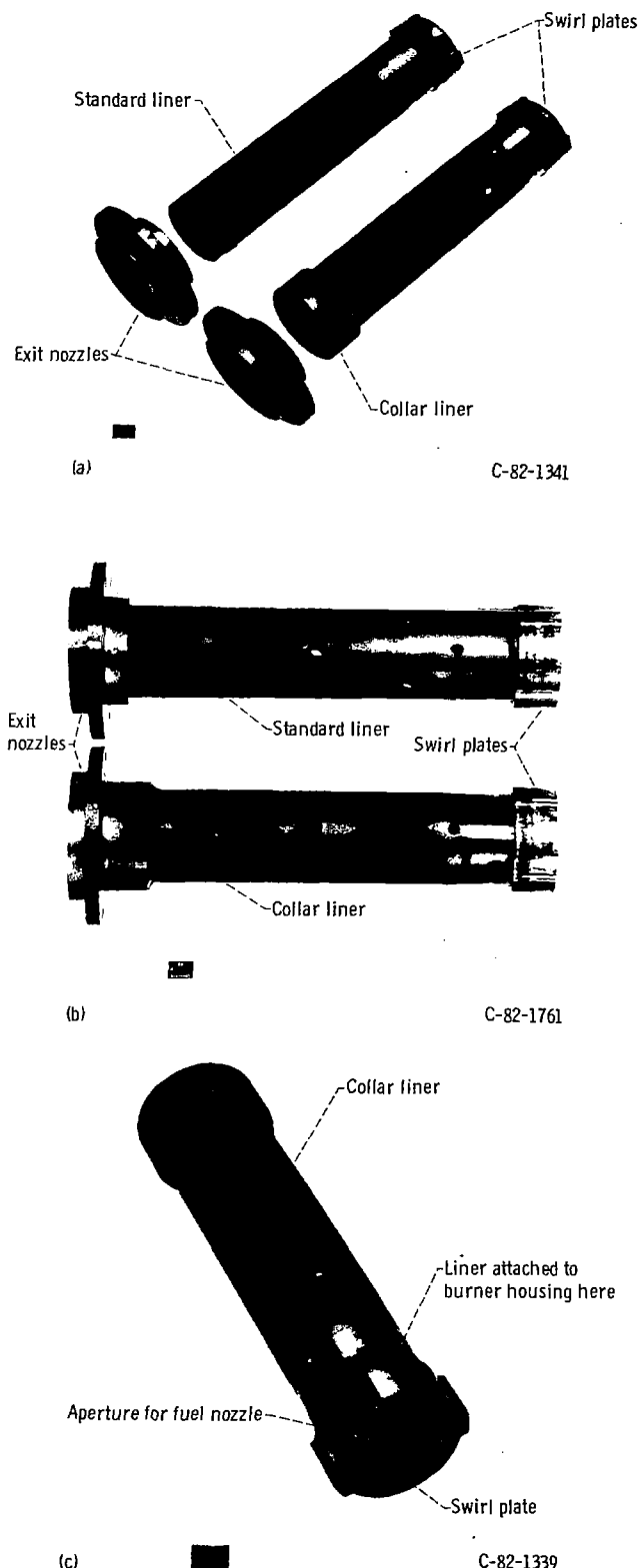


Figure 18. — Standard burner liner and modified collar burner liner.

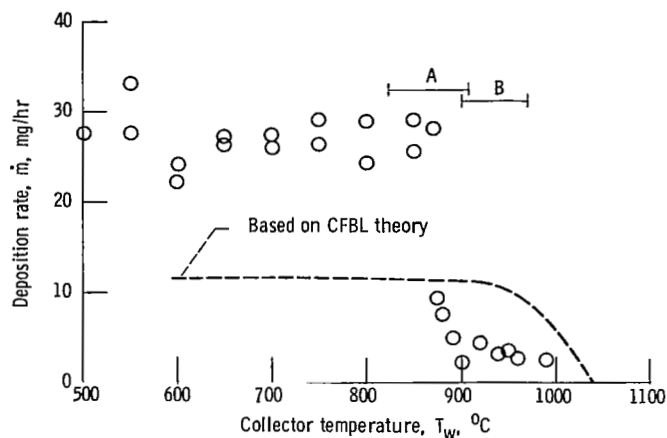


Figure 19. — Effect of collector temperature on deposition rate from Na_2SO_4 -seeded burner using collar liners. (Bracketed data are the deposition results on thermal-barrier-coated collectors A and B.)

feature has to be attributed to the use of the collar liner (compare fig. 19 with fig. 11). But it is not clear why the liner modification should affect deposition rates this way. As will be seen, the plateau is a feature of all of the data where collar liners were used. However, above the melting point of Na_2SO_4 (884°C), the experimental data fall off sharply instead of descending exponentially near the dewpoint as CFBL deposition rate theory would predict. The dashed line in figure 19 represents calculated deposition rates based on the CFBL theory. Actually just two parameters from the theoretical curve, the plateau value and the dewpoint, are needed to closely approximate the entire curve by equation (2). Table II summarizes the input for the CFBL computer program, and appendix C is a simplified example of the calculation using the Na_2SO_4 case input to illustrate the use of the theory. Appendix D contains a sensitivity analysis associated with the more elaborate calculations in the computer program.

Synthetic Sea Salt Results

Deposition on collectors exposed to synthetic-sea-salt-seeded combustion gases was investigated as sea salt is often the form of the contaminant in turbine engines, particularly marine engines. The standardized composition of synthetic sea salt (ASTM D-1141-52) is listed in table I. Figure 20 contains the deposition rate data. The sea salt case is more complex than a single-component solution because more than one species can deposit. The experimental points in figure 20 represent the sum total of these deposits. The dashed line in figure 20 represents the predicted values of deposition rate for Na_2SO_4 only. Under the conditions of these experiments (table II), the bulk of the deposit is expected to be Na_2SO_4 . A schematic representation of the relative deposition rates for all components of the deposits based on the conditions

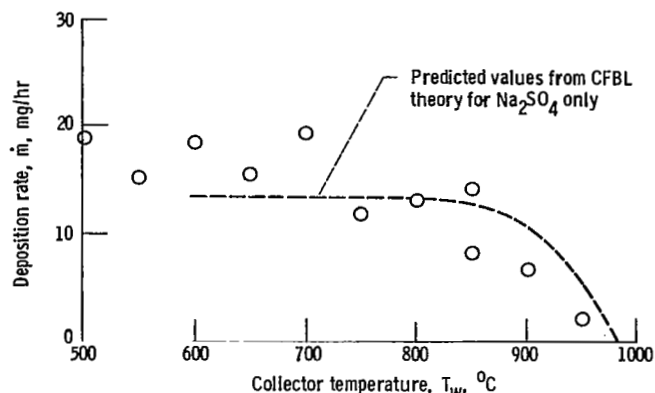


Figure 20. — Effect of collector temperature on deposition rate from synthetic-sea-salt-seeded burner.

similar to those listed in table II for sea salt is given in figure 21. The dewpoint and transition temperatures were calculated by the NASA CEC computer program (ref. 45). In figure 21 the relative deposition rates were based on the relative amounts of the condensed phases calculated by the CEC program without considering transport through a boundary layer. This procedure should yield a rough approximation of relative deposition rates provided that the transport properties of the vapor species containing the elements of the condensed phases are of the same order of magnitude.

The X-ray diffraction (XRD) analysis of the deposits on collectors exposed at 550° , 650° , 750° , and 850°C revealed the presence of Na_2SO_4 and MgO . The MgO line intensities decreased relative to those of Na_2SO_4 with decreasing collector temperature. But MgO was still present in deposits from collectors exposed at the two lowest temperatures (550° and 650°C), where according to figure 21 MgSO_4 should be the stable magnesium phase.

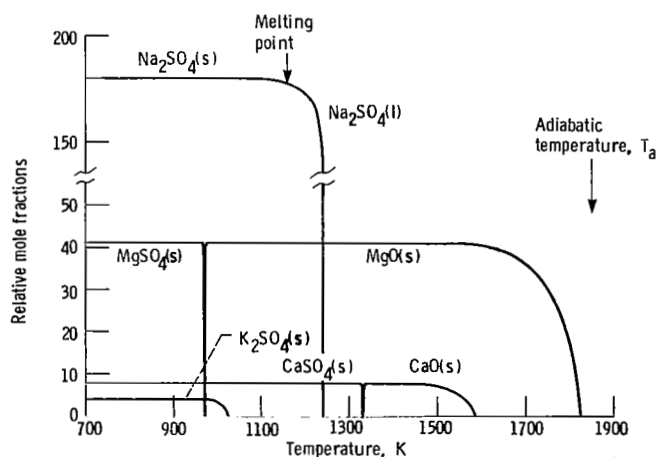
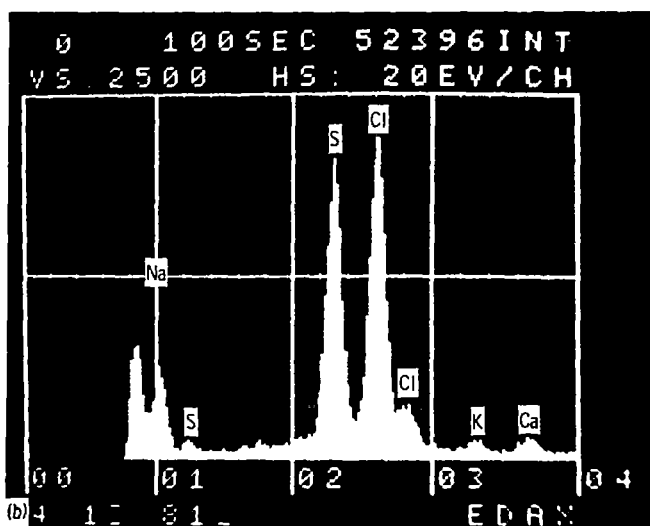
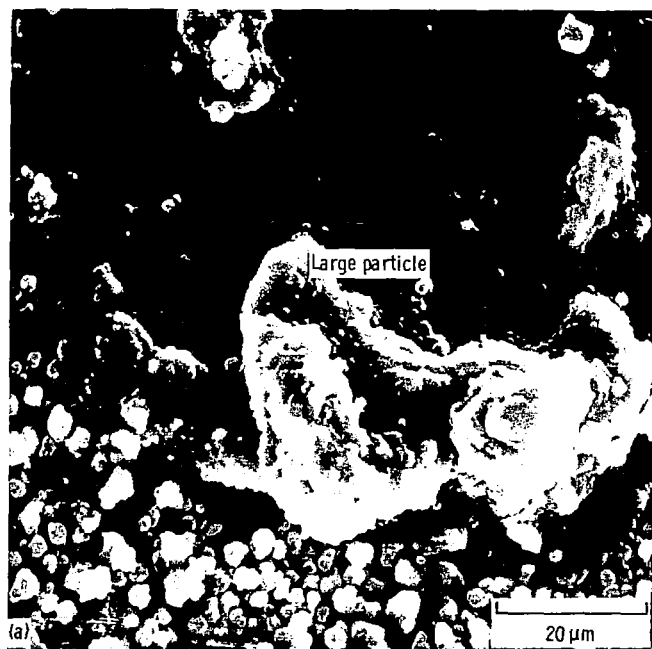


Figure 21. — Relative deposition rates based on the CEC computer program from synthetic sea salt for all components of deposit. Note break in ordinate axis.

Apparently the kinetics are such that condensed MgO , which is the stable species at higher temperatures, does not convert to MgSO_4 at the collector temperature in the given time frame. Energy dispersive spectroscopy (EDS) analyses of deposits on collectors exposed at 500° and 950° C reveal those elements expected from figure 21, including potassium in the 500° C deposit. In the latter, however, isolated and relatively large particles have been observed. Figure 22 shows an example of an isolated



(a) SEM micrograph showing an occasional large particle.
(b) EDS spectra of particle in (a) showing presence of chlorine.
Figure 22. – Morphology of deposit from synthetic-sea-salt seeded burner.

large particle over a field of smaller, more typical particles. The EDS spectrum of this particle indicates the presence of all of the elements expected in a deposit from a sea-salt-seeded run plus the $K\alpha$ and $K\beta$ lines for chlorine, which were not expected.

K_2SO_4 Results

Before the K_2SO_4 tests began, additional collar liners had been fabricated to facilitate the testing of the hypothesis that liner-to-liner variation would be eliminated by the collar modification. Another consideration at this time was to test with a salt whose melting point was above its dewpoint. Thus, instead of a liquid deposit near the dewpoint, the deposit would be solid, allowing us to test the speculation that the anomaly observed near the dewpoint from tests seeded with Na_2SO_4 may be related to the deposit being a liquid at these temperatures. Under the conditions of these experiments an alkali salt whose melting point (1076° C) exceeds its dewpoint is K_2SO_4 . During the testing with K_2SO_4 a combustion air preheater was installed on the burner rig. Thus the K_2SO_4 test was divided into two parts, with and without preheated combustion air. Both parts involved several collar liners.

Figure 23 presents the deposition rates for K_2SO_4 -seeded runs using ambient combustion air and four different collar liners. Figure 24 presents the analogous data for combustion air preheated to 253° C. The dashed lines in these figures are the CFBL predicted values. The input to the program for the K_2SO_4 case is given in table II. Liner-to-liner variation effects on the deposition rates were within the scatter of the data. Data at the high-temperature end of the curve (near the dewpoint) agreed better with theoretical predictions than did the Na_2SO_4 data, but the descent to the dewpoint was still not as theory predicts.

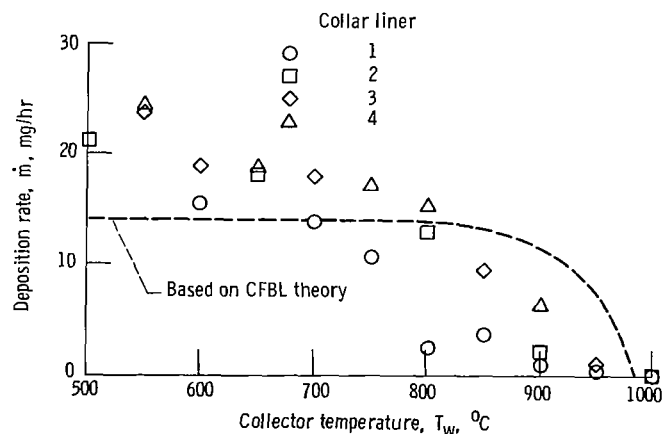


Figure 23. – Effect of collector temperature on deposition rate from K_2SO_4 -seeded burner using ambient combustion air and four different collar liners.

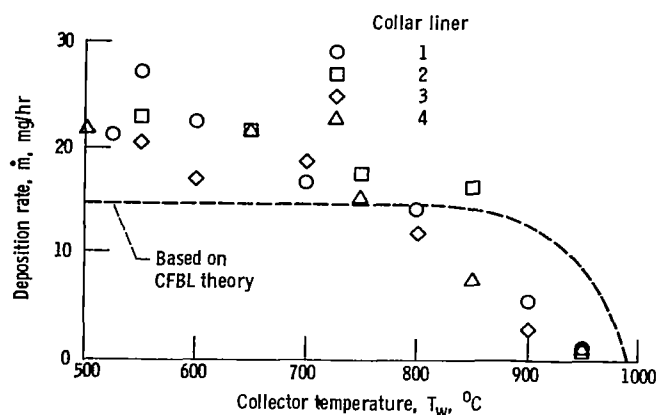


Figure 24. – Effect of collector temperature on deposition rate from K_2SO_4 -seeded burner using preheated combustion air ($253^\circ C$) and four different collar liners.

The deposits on collectors heated at 650° , 750° , and $850^\circ C$ were analyzed by XRD. The only phase detected in any of the deposits was K_2SO_4 . The deposits on the collectors heated at 500° and $950^\circ C$ were analyzed by EDS. Only potassium and sulfur were detected.

NaCl and $NaNO_3$ Results

To further test the CFBL deposition rate theory, two other sodium salts were selected to seed the burner. Sodium chloride was chosen as it is the main constituent of sea salt, and it will deposit only as Na_2SO_4 without any Mg or K compounds. A more direct comparison can be made between Na_2SO_4 - and NaCl-seeded deposition rates with equivalent sodium concentration than can be made between Na_2SO_4 and sea salt. The other sodium salt chosen was $NaNO_3$. This salt provides the sodium required for Na_2SO_4 deposition but without the presence of chlorine. The effect of chlorine on deposition is discussed later.

Figure 25 shows the NaCl data. The dashed line again was calculated by using the CFBL program. Table II lists the input for the computer program. As in the case of the Na_2SO_4 tests (figs. 11 and 19), the NaCl runs (fig. 25) yield low deposition rates at collector temperatures beyond the melting point of Na_2SO_4 . Again there is no liner-to-liner variation beyond the scatter in the data.

Figure 26 presents the deposition data from the Na_2NO_3 tests. As with all of the single-component sodium salts, low deposition rates were obtained for liquid deposits. There is some indication in the data of a maximum near $850^\circ C$. The dashed curve represents the predicted values from the CFBL program, the input of which is listed in table II. The only phase detected in the deposit on collectors exposed at 500° , 800° , and $900^\circ C$ was Na_2SO_4 . EDS analysis revealed only the elements sodium and sulfur in deposits from collectors exposed at 500° and $900^\circ C$.

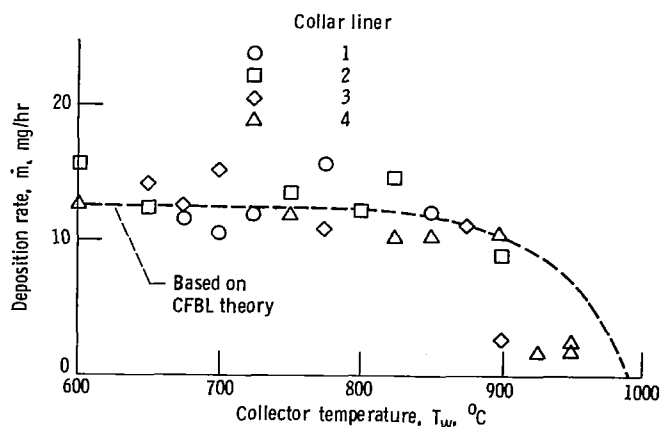


Figure 25. – Effect of collector temperature on deposition rate from NaCl-seeded burner using preheated combustion air ($259^\circ C$) and four different collar liners.

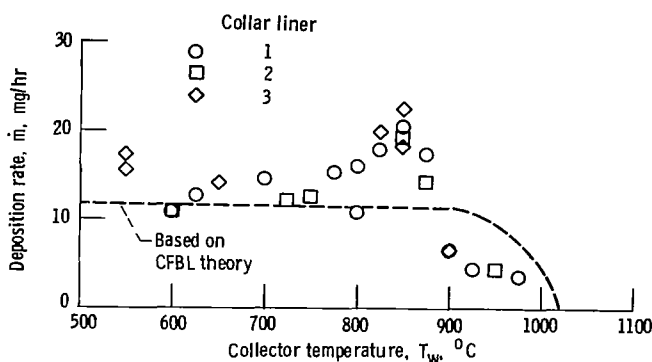


Figure 26. – Effect of collector temperature on deposition rate from $NaNO_3$ -seeded burner using preheated combustion air ($259^\circ C$) and three different collar liners.

The $NaNO_3$ and NaCl runs were made with about the same sodium concentrations in the combustor as well as comparable values of all of the other test parameters. The only deposit detected in both cases was Na_2SO_4 . Yet the predicted dewpoint for the $NaNO_3$ run ($1039^\circ C$) was 50 degrees higher than that for the NaCl run ($989^\circ C$). These values are consistent with the experimental values in figures 25 and 26, but the low deposition rates above the melting point of Na_2SO_4 preclude an accurate determination. Although equilibrium thermodynamic calculations predict that chlorine ought to lower the dewpoint of Na_2SO_4 condensation, it ought not to affect the plateau deposition rate, all other parameters being equal. This point is consistent with the experimental data in figures 25 and 26.

Supplementary Tests and Results

A number of supplementary tests were conducted to aid in interpreting the deposition rate data. One set of

tests were directed toward explaining the low deposition rates observed at collector temperatures above the melting point of Na_2SO_4 in sodium-salt-seeded runs. Because the distribution of deposited salt on a stationary collector can supply information on the deposition process, a preliminary effort was made in this area. The spray droplet size distribution of the Na_2SO_4 solution was measured to examine the assumption that this salt completely vaporizes in the combustor. Finally, calorimetry tests were conducted to experimentally determine the heat transfer Nusselt number, from which the main-stream turbulence factor can be extracted.

Deposition of Na_2SO_4 Above its Melting Point

Observed deposition rates below those predicted for collector temperatures above the melting point of Na_2SO_4 (884°C) suggest the possibility that liquid Na_2SO_4 is somehow being lost from the collectors. This hypothesis is supported somewhat by the K_2SO_4 data, where the melting point of K_2SO_4 exceeds its dewpoint and the deposition rates near the dewpoint for comparable concentrations in the combustor are much closer to those predicted for this salt than in the case of Na_2SO_4 (compare fig. 19 with figs. 23 and 24). Several possible mechanisms for the loss of liquids are (1) flow from the collector to the adjacent ceramic spacers, (2) spalling during the liquid-to-solid phase transition when the collector is cooled upon the completion of the run, and (3) blowoff by the aerodynamic shear force of the high-velocity burner gases. All three possibilities were investigated.

The procedure for testing the first possible mechanism, flow from the collector to the spacers, was as follows: Standard 30-minute deposition runs were made with collector temperatures well below the melting point of Na_2SO_4 so as to insure a large deposit. After weighing to determine the amount of deposit, these collectors were reinserted into the rig but this time with virgin Al_2O_3 spacers. These collector assemblies were then exposed to unseeded burner gases (salt free) at collector temperatures of 850°C (control tests) and 900°C (above the melting point of Na_2SO_4) for 30 minutes. The Al_2O_3 spacers were then analyzed for sodium, and these analyses were compared with the sodium analysis of as-received Al_2O_3 spacers (blanks). No difference in the sodium content was detected between any of the exposed spacers and the blank spacers. The sodium content averaged 0.08 ± 0.03 percent. Thus either Na_2SO_4 was not lost from the collector by flowing onto the spacers, or any salt that may have flowed onto the spacers was completely evaporated. It should be noted that the temperature of the spacer near the collector was always higher than the temperature of the collector (fig. 4). However, there was a discontinuity between the spacers

and the collector, which would tend to restrict flow from one component to the other.

In these tests the collectors with Na_2SO_4 deposits held at 900°C in the salt-free combustion gases lost most of their deposit (84 to 92 percent), those held at 850°C lost much less (11 to 20 percent). Some of the small loss at 850°C may be due to evaporation. These results provide further evidence supporting the hypothesis that liquid deposits on the collectors were lost, giving the impression of low deposition rates.

To test the possibility of spalling as a loss mechanism, a burner rig run was made where Na_2SO_4 was deposited at a collector temperature well below the melting point of Na_2SO_4 . This collector with its deposit was then placed in a platinum crucible and heated overnight in a furnace at 900°C . About 13 percent of the deposit was lost (probably through evaporation). Upon cooling, no salt particles were observed in the crucible, and the crucible did not undergo a measurable weight change. Therefore spalling alone cannot account for the difference between the predicted and measured rates in the deposition curve above the melting point of Na_2SO_4 .

The third mechanism, aerodynamic blowoff by the shear force of the high-velocity gas stream, must (by the process of elimination) be the major loss mechanism. If indeed this is the process, it occurs in 5 minutes or less, because a collector with a large deposit of Na_2SO_4 lost most of its deposit when reheated to 900°C in a salt-free gas stream for only 5 minutes. To positively confirm this loss mechanism, yet another set of tests was conducted. It might be expected that the liquid deposit could be retained if the surface of the collector were porous or rough. A collector composed of a thin layer of ceramic material on a metallic substrate could provide such a surface and yet allow for internal cooling. A thermal barrier coating would apparently meet these requirements (ref. 47). The substrate alloy chosen was 304 stainless steel and the bond and barrier coating specifications were those suggested by Stephan Secura of NASA Lewis (private communication) and are given in table III. Two barrier-coated collectors were fabricated and labeled A and B.

The overall dimensions of the thermal-barrier-coated collectors (fig. 27), were the same as those of the Pt-Rh collectors (fig. 5). Determining the surface temperatures of the thermal-barrier-coated collectors was a problem. A calibration run in salt-free combustion gases was made for each of the two ceramic-coated collectors. In the calibration runs the perforated stem of the collector assembly was replaced with a solid stem and the perforated cap on the top spacer was replaced with a solid cap (fig. 5). Thus no internal cooling could occur, not even by convection. The collector temperature was varied by changing the fuel-to-air ratio of the burner. It was then assumed that without internal cooling the temper-

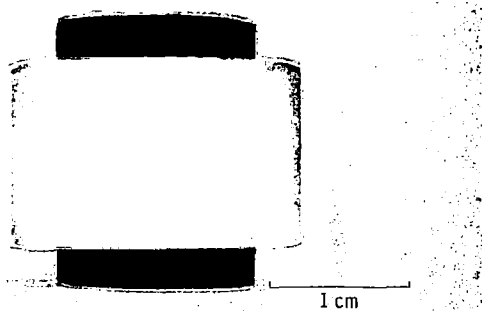


Figure 27. — Thermal-barrier-coated collector after exposure in Na_2SO_4 -seeded burner. (Salt has been washed off and quantitatively analyzed.)

ature sensed by the thermocouple embedded in the wall of the collector would be the same as the surface temperature under steady-state conditions. An optical pyrometer calibrated against this thermocouple could then be used to determine the surface temperature of the internally cooled barrier-coated collector in the subsequent deposition runs. A complication arose during the calibration runs when a temperature gradient was observed via the optical pyrometer from the leading surface of the collector to the trailing surface, even though the collector was spinning at 230 rpm. Increasing the rotational speed did not eliminate this gradient, although it was decreased somewhat. Because of the temperature gradient the mean optical pyrometer reading was calibrated against the thermocouple.

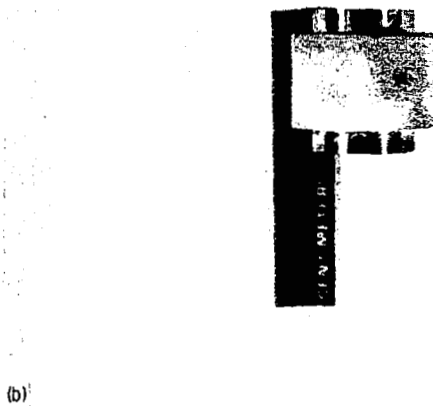
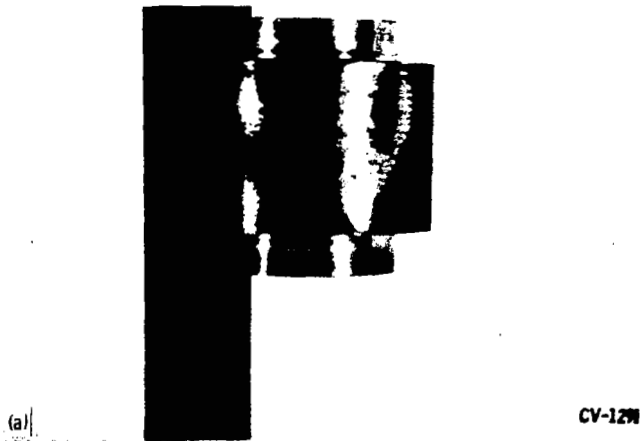
After calibration these collectors were exposed to Na_2SO_4 -seeded combustion gases for 30 minutes. The salt deposited on these collectors was dissolved in hot distilled water. After filtering, the filtrate was analyzed for sodium by atomic absorption spectroscopy (AAS). The filter paper, meanwhile, was ignited and its residue was measured and subtracted from the loss in weight of the collectors due to the washing. This difference should be the amount of Na_2SO_4 deposited, and it agreed well with the AAS analysis. Thus for collector A the net weight change was 16.3 mg as compared with the AAS value of $5.2 \text{ mg} \pm 10 \text{ percent Na}$, equivalent to 16.1 mg as Na_2SO_4 . For collector B the numbers are 13.9 mg and 17.3 mg (as Na_2SO_4) for the weight change and AAS analysis, respectively. The two types of determinations for the amount of deposit were then averaged and plotted in figure 19. A temperature range was given to reflect temperature uncertainties. The amount of deposit on thermal-barrier-coated collectors was much greater than that on the Pt-Rh collectors exposed at the same temperatures and salt concentration. In fact the deposits on the coated collectors represent deposition rates close to the plateau values of the experimental data. Although the deposition rates from ceramic-coated collectors and the lower temperature data from Pt-Rh collectors ex-

ceeded the predicted values, these and the previously presented results strongly suggest that liquid deposits of Na_2SO_4 are blown off smooth surfaces in the high-velocity gas stream of the Mach 0.3 burner rig.

Salt Distribution with no Rotation

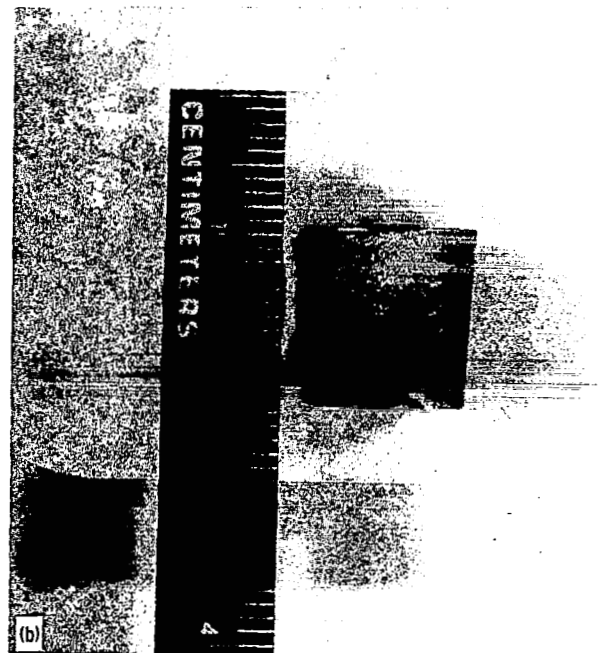
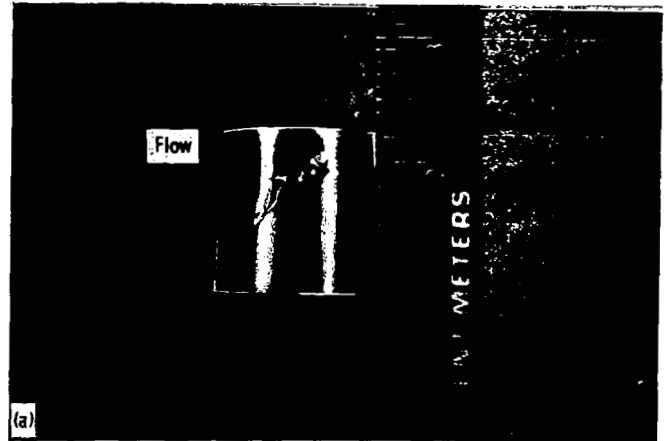
To gain further insight into the deposition process, it would be helpful to experimentally determine the salt distribution on stationary targets in the burner rig. No quantitative method has been devised as yet for measuring the salt distribution on the standard collector, and only qualitative data were gathered from tests using these collectors. Standard deposition tests with the combustor seeded with Na_2SO_4 were conducted at collector temperatures of 650° , 900° , and 950° C , except that the collectors were not rotated. The collectors were orientated so that the surface with the thermocouple embedded in its wall faced the gas stream, and therefore the three test temperatures represent leading surface temperatures of the collector.

A magnified view of the leading surface of a standard collector heated at 900° C is shown in figure 28(a). The feather pattern gives the impression of a liquid film having been blown around the sides of the collector, which is consistent with the findings discussed in the previous section. Salt was not readily visible on the trailing surface of this collector but was detected by XRD. The collector heated at 950° C had a salt pattern similar to that of the 900° C collector, but the features were not as sharp, reflecting the smaller amount of salt deposited on this collector (4 mg as compared with 9.5 mg). The collector heated at 650° C had a large amount of an off-white deposit (18.9 mg) around its entire surface that seemed fairly uniform except for a dark area on the leading surface that appeared more granular and thicker (fig. 28(b)). An attempt to obtain quantitative salt distribution data was made by using the sleeve collector of the previous program (figs. 1 and 2). The plan was to slice each thin-wall sleeve with its deposit into strips, weigh each strip, wash off the salt, and weigh the strip again. Unfortunately the slicing caused some of the salt to spall. It could not be shown that the loss was proportional to the amount originally there, thereby prohibiting the determination of even a relative distribution. Thus with either type of collector only preliminary results have been obtained to date. The sleeve collectors were not designed to be internally cooled. So to provide fuel-to-air ratios comparable to those used with the standard collector, the collector assembly had to be located about 10 cm (4 in.) from the exit nozzle (as compared with the 1-cm (0.4-in.) standard distance). The collector temperature in this case could only be altered by adjusting the fuel-to-air ratio. In the salt distribution runs with the standard collectors the fuel-to-air ratio was



(a) Leading surface whose temperature was at 900° C.
(b) Leading surface whose temperature was at 650° C

Figure 28. - Standard collectors with deposits from Na₂SO₄-seeded burner. (Collectors were not rotated while exposed to the combustion gases.)



(a) Right side of collector whose leading surface was at 900° C. This collector's left side had a similar salt buildup.
(b) Leading surface of a collector whose temperature was at 800° C.

Figure 29. - Sleeve collectors with deposits from Na₂SO₄-seeded burner. (Collectors were not rotated while exposed to the combustion gases.)

0.0450. The ratios for the sleeve collector runs were 0.0430 and 0.0493 for leading surface temperatures of 800° and 900° C, respectively. All of the other burner parameters remained the same as before. In the sleeve collector runs the trailing surface temperatures of the 800° and 900° C collectors were 756° and 840° C, respectively.

Figure 29 shows the sleeve collectors with their salt deposits. For both collectors more salt appears to have been deposited on the leading surface than on the trailing surface. A distinct buildup of salt is noticeable on either side of the collector heated at 900° C, again indicating

movement of a liquid deposit on a smooth surface in a high-velocity gas stream. Note that 900° C (the leading-surface temperature) is above the melting point of Na₂SO₄ and 840° C (the trailing-surface temperature) is below its melting point. Between the two surfaces, apparently on the sides, the temperature was at the melting point. Thus liquid Na₂SO₄ on the surface of the collector facing the gas stream flowed around to the sides, where it solidified. Continuous flow and

solidification then caused the salt buildup shown in figure 29.

Both sleeve collectors were sliced into four pieces, representing leading and trailing quadrants and left and right quadrants. Only 41 percent of the deposit was retained after slicing the sleeve heated at 900° C; 65 percent was retained on the sleeve heated at 800° C. Of the retained salt on the sleeve heated at 900° C, 50 percent was on the leading quadrant, 9 percent on the trailing quadrant, and the remaining 41 percent on the two side quadrants. The breakdown on the sleeve heated at 800° C was 90 percent on the leading quadrant, 2 percent on the trailing quadrant, and the remaining 8 percent on the two side quadrants.

If the deposition mode was purely vapor diffusion through the boundary layer, the salt distribution on the collector would be dependent on the Reynolds number. For the Reynolds number in these experiments ($Re = 1.3 \times 10^4$) the fraction of salt on the front of a cylinder should be between 0.65 and 0.70 (ref. 48). The amount of retained deposit on the projected area of the 800° C sleeve collector was about 94 percent (i.e., 90 percent from the front quadrant and 2 percent from each of the two side quadrants). In this analysis liquid flow was not a consideration nor was the temperature gradient on the collector. The latter was within the plateau region of the deposition curve, where rate is not sensitive to the temperature of the collector. Thus the observation that more than 70 percent of the deposit was on the leading surface suggests that inertial impaction of salt droplets played a role in the deposition process.

Salt Spray Size Distribution and Droplet Survival

It has been assumed until now that all of the salt sprayed into the combustor vaporizes. This section examines that assumption by describing the determination of the salt spray size distribution and the estimation of the time for complete vaporization of the salt in the combustor. Na_2SO_4 was considered for this study as it has the lowest vapor pressure of all of the salts tested.

The salt-atomizing injector and its position in the combustor is shown in figure 14(a). The droplet size distribution was measured by using this injector and a Malvern droplet size analyzer. Detailed descriptions of the instrument and the principles of its operation are given in the literature (refs. 49 and 50) and are only briefly presented here. The technique is based on the Fraunhofer diffraction of a parallel beam of monochromatic light by the moving droplets. A Fourier transform lens focuses a stationary light pattern on a multielement photodetector, which measures the diffracted light energy distribution. The light energy distribution is unique for a unique droplet or particle size distribution. A minicomputer program translates the light energy distribution into its corresponding size dis-

tribution by assuming a Rosin-Rammler size distribution function. The Rosin-Rammler distribution density function by weight fraction is given by

$$P(d_s) = \frac{w d_s^{w-1}}{(PE)^w} \exp \left[- \left(\frac{d}{PE} \right)^w \right] \quad (3)$$

for droplet or particle diameter d_s . The parameters of this distribution function are PE and w ; the former is characteristic of the size, and the latter is related to the width of the distribution and is large for a narrow distribution. The computer determines the values of these two parameters that best fit the data (i.e., to minimize the error E).

The experimental setup is schematically shown in figure 30. Figure 31 consists of the computer printouts for a typical distilled-water run and a typical Na_2SO_4 solution run. Both runs used 34-kPa (5-psi) atomizing air gage pressure and had the laser beam intercept the spray at the radial center and at an axial distance of 3 cm (1.2 in.) from the probe. The parameters of the distribution function are PE and w , as defined above. The error value is E and represents the goodness of fit. Column 1 shows the 15 size bands in micrometers; column 2 shows the content of each band in weight percent; column 3 shows the cumulative weight fraction; column 4 shows the number percent for each size band; column 5 shows the computed light energy distribution; and column 6 presents the corresponding measured values. Data from figure 31 are presented as histograms in figure 32. Adding Na_2SO_4 to the distilled water produced a smaller droplet

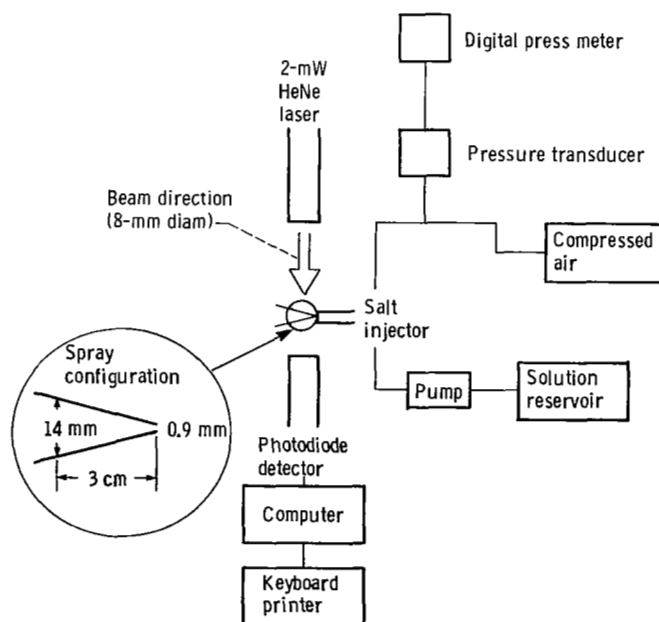


Figure 30. — Schematic representation of the experimental array for droplet size distribution experiments.

> PE = +40.0 W = +5.2 E = 00461784

D = +562.86 > +261.71 P = +0.00% R = +100.00% N = +0.00% C = 0094 A = 0227
D = +261.71 > +160.29 P = +0.00% R = +100.00% N = +0.00% C = 0153 A = 0454
D = +160.29 > +112.86 P = +0.00% R = +100.00% N = +0.00% C = 0253 A = 0568
D = +112.86 > +84.29 P = +0.00% R = +100.00% N = +0.00% C = 0399 A = 0682
D = +84.29 > +64.57 P = +0.00% R = +100.00% N = +0.00% C = 0632 A = 0796
D = +64.57 > +50.29 P = +3.74% R = +96.26% N = +0.61% C = 0969 A = 1250
D = +50.29 > +38.86 P = +38.58% R = +57.69% N = +13.56% C = 1425 A = 1364
D = +38.86 > +30.29 P = +36.72% R = +20.97% N = +27.65% C = 1864 A = 1705
D = +30.29 > +23.71 P = +14.59% R = +6.38% N = +23.06% C = 2046 A = 2047
D = +23.71 > +18.57 P = +4.55% R = +1.83% N = +14.98% C = 1742 A = 1819
D = +18.57 > +14.57 P = +1.31% R = +0.52% N = +8.96% C = 1095 A = 1364
D = +14.57 > +11.43 P = +0.37% R = +0.15% N = +5.31% C = 0683 A = 0909
D = +11.43 > +9.14 P = +0.10% R = +0.05% N = +2.91% C = 0537 A = 0227
D = +9.14 > +7.14 P = +0.03% R = +0.01% N = +1.93% C = 0423 A = 0000
D = +7.14 > +5.71 P = +0.01% R = +0.00% N = +1.03% C = 0311 A = 0000

(a)

> PE = +25.0 W = +31.2 E = 00827286

D = +562.86 > +261.71 P = +0.00% R = +100.00% N = +0.00% C = 0042 A = 0000
D = +261.71 > +160.29 P = +0.00% R = +100.00% N = +0.00% C = 0070 A = 0000
D = +160.29 > +112.86 P = +0.00% R = +100.00% N = +0.00% C = 0117 A = 0000
D = +112.86 > +84.29 P = +0.00% R = +100.00% N = +0.00% C = 0189 A = 0000
D = +84.29 > +64.57 P = +0.00% R = +100.00% N = +0.00% C = 0310 A = 0000
D = +64.57 > +50.29 P = +0.00% R = +100.00% N = +0.00% C = 0503 A = 0000
D = +50.29 > +38.86 P = +0.00% R = +100.00% N = +0.00% C = 0811 A = 0000
D = +38.86 > +30.29 P = +0.00% R = +100.00% N = +0.00% C = 1229 A = 0818
D = +30.29 > +23.71 P = +82.48% R = +17.52% N = +69.32% C = 1701 A = 1637
D = +23.71 > +18.57 P = +17.51% R = +0.01% N = +30.64% C = 2043 A = 2047
D = +18.57 > +14.57 P = +0.01% R = +0.00% N = +0.03% C = 1893 A = 1637
D = +14.57 > +11.43 P = +0.00% R = +0.00% N = +0.00% C = 1142 A = 1023
D = +11.43 > +9.14 P = +0.00% R = +0.00% N = +0.00% C = 0344 A = 0204
D = +9.14 > +7.14 P = +0.00% R = +0.00% N = +0.00% C = 0324 A = 0000
D = +7.14 > +5.71 P = +0.00% R = +0.00% N = +0.00% C = 0463 A = 0000

(b)

(a) Distilled water.

(b) Na₂SO₄ solution (6.16 g/liter).

Figure 31. – Computer printouts for typical distilled water and Na₂SO₄ solution droplet size determination. Atomizing air gage pressure, 3.4×10^4 Pa (5 psi); axial distance from probe, 3 cm (1.2 in.).

size spray for the same atomizing air pressure and also decreased the spread of the distribution.

To determine the time for complete vaporization of the spray, it was assumed that the water in the solution droplet would vaporize first, leaving just the salt, which would form molten droplets whose size would be related to its density and its original concentration in the solution. The volume of a drop of solution is

$$V_s = \frac{\pi d_s^3}{6} \quad (4)$$

The volume of a drop of Na₂SO₄ is

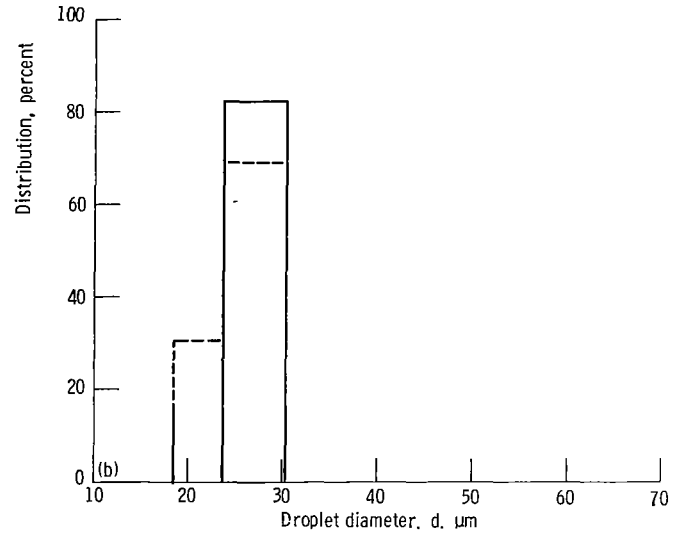
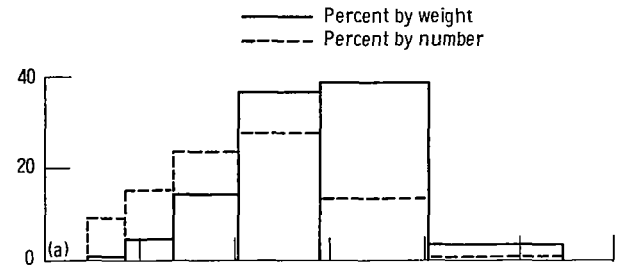
$$V_p = \frac{V_s N}{\rho_p} \quad (5)$$

and

$$\frac{\pi d_p^3}{6} = \frac{\pi d_s^3 N}{6 \rho_p} \quad (6)$$

$$d_p = d_s \left(\frac{N}{\rho_p} \right)^{1/3} \quad (7)$$

The Sauter mean diameter SMD calculated from the Na₂SO₄ solution size distribution parameters was 24.6 μ m:



(a) Distilled water. Sauter mean diameter, 34.6 μ m.

(b) 6.16-g/liter Na₂SO₄. Sauter mean diameter, 24.6 μ m.

Figure 32. – Droplet size distribution for distilled water and 6.16-g/liter Na₂SO₄ solution. Atomizing air pressure, 1.36×10^5 Pa (5 psig); axial distance from probe, 3 cm (1.18 in.).

$$\text{SMD} = \frac{\text{PE}}{\Gamma[1 - (1/w)]} \quad (8)$$

where PE = 25, $w = 31.2$, and Γ is the gamma function. The SMD is the monodisperse drop size, which has the same surface area as the given spray. When this mean is used for d_s in equation (7), the corresponding Na₂SO₄ drop size d_p is 3.2 μ m, where N is 6.2×10^{-3} g/cm³ and ρ_p is taken as 2.689 g/cm³. The Na₂SO₄ solution drop diameter was translated into time for complete vaporization as shown below.

The method first considers the time t_s for the complete vaporization of the water from a solution droplet of size equal to the SMD (24.6 μ m) down to the droplet size of the incorporated salt after the water has evaporated (3.2 μ m). Then the time for the vaporization of this salt t_p is calculated. The sum of these two vaporization times is considered the total vaporization time characteristic of the Na₂SO₄ solution droplet size distribution. A simplifying assumption, which introduces a negligible error, has been made in these calculations. It has been

assumed that the mass transfer Nusselt number is 2. Details are presented in appendix E.

Vaporization of water:

$$t_{H_2O} = \frac{\rho_{H_2O} c_{p,air}}{\lambda_{air}} \frac{1}{\ln(1+B_h)} \frac{(d_{H_2O,in}^2 - d_{H_2O,p}^2)}{8} \quad (9)$$

and the heat transfer parameter B_h is

$$B_h = \frac{c_{p,air}(T_0 - T_w)}{\Lambda + c_{p,H_2O}(T_w - T_{in})} \quad (10)$$

The droplet surface temperature never reaches the gas-stream temperature due to the cooling effect Λ of the vaporization. The problem is to calculate the proper value for T_w in equation (10). This calculation is accomplished by an iterative process using the following relationship as a result of the coupling between heat and mass transfer:

$$(1 + B_m)^{1/Le} = 1 + B_h \quad (11)$$

where

$$Le = Pr/Sc \quad (12)$$

The Prandtl number can be obtained from the literature (ref. 51), and the Schmidt number can be calculated as shown in appendix B. Equation (11) states the balance between the vaporization rate due to the heat transferred to the droplet from the gas stream and the diffusion rate of the vaporized molecules from the surface of the droplet out into the gas stream. The mass transfer parameter is

$$B_m = \frac{\omega_{H_2O,w} - \omega_{H_2O,\infty}}{1 - \omega_{H_2O,w}} \approx \frac{\omega_{H_2O,w}}{1 - \omega_{H_2O,w}} \quad (13)$$

where the water vapor in the gas stream is considered negligible when compared with $\omega_{H_2O,w}$. The mass fraction of the water vapor at the surface of the solution can be calculated from the vapor pressure of water at T_w by using the relationship

$$\omega_{H_2O,w} = \frac{p_{vap,H_2O} M_{H_2O}}{(p_0 - p_{vap,H_2O}) M_{air} + p_{vap,H_2O} M_{H_2O}} \quad (14)$$

The influence of the salt on the water vapor pressure of the solution droplet is considered to be negligible.

The procedure is now to repeatedly adjust T_w in equation (10) until the equality in equation (11) is

satisfied. Note that $\omega_{H_2O,w}$ in equation (14) must be recalculated for each choice of T_w . Upon the satisfactory completion of this iteration, the proper value for B_h is substituted into equation (9). Using the SMD determined above, the time for the complete vaporization of the water in the Na_2SO_4 solution droplet was calculated to be $t_{H_2O} = 2.5$ msec at $T_w = 352$ K, $T_0 = 1736$ K, and $p_0 = 1.068$ atm.

The time required for the vaporization of the molten Na_2SO_4 residue is considered next.

Vaporization of Na_2SO_4 :

$$t_p = \frac{\rho_p c_{p,air}}{\lambda_{air}} \frac{1}{\ln(1+B_h)} \frac{d_{p,in}^2}{8} \quad (15)$$

The same iterative process employed for the water portion of the solution is used to calculate the vaporization of the remaining Na_2SO_4 droplet where the appropriate values for Na_2SO_4 are inserted in equations (10) to (15), the subscript H_2O being replaced by Na_2SO_4 . This process yields a t_p of 9.6 msec. Thus the total time characteristic of the vaporization of Na_2SO_4 solution droplets in the combustor is $t_{H_2O} + t_p = 12.1$ msec.

Solution droplet interaction was not a consideration in these calculations because of the dilute loading in the gas stream. Thus, with the SMD value calculated above, there were about 70 droplets per cubic centimeter of gas, or stated another way, the distance between droplets was almost 100 droplet diameters.

The residence time of the spherical droplets in the combustor is

$$t_r = \frac{l}{U_{mix,c}} \quad (16)$$

where

$$U_{mix,c} = \frac{\dot{W}_{mix} RT}{p_0 M_{mix} S} \quad (17)$$

At 1736 K and 1.07 atmospheres pressure, $t_r = 2.3$ msec. For a more rigorous calculation of residence time in the combustor, see the discussion section and appendix E, where consideration is given to the acceleration of the droplets to the main-stream velocity.

The residence time of the solution droplets in the combustor is about only 0.2 times that required for complete vaporization in the case of Na_2SO_4 . Thus droplets can be expected to survive travel through the combustor and, if large enough, to inertially impact onto the collector. Of the salts tested, Na_2SO_4 had the lowest vapor pressure. The higher vapor pressures of the other

salts would decrease the time for their vaporization. For the purpose of illustration, if the droplet size distribution of an NaCl solution were identical to that of the Na₂SO₄ solution, t_s would also be identical (2.5 msec), but t_p would be <0.4 msec. Thus for the NaCl solution example, the total vaporization time would be essentially the time for the vaporization of the water, as the time for the salt itself to vaporize was small by comparison.

Calorimetry Experiment

An important, but difficult to calculate, parameter in the deposition flux equation is the main-stream turbulence factor, which is a premultiplier in equation (1) and so directly affects the mass flux. Because free-stream turbulence influences heat and mass transfer, an experimentally derived Nusselt number would contain the F_{turb} effect. The turbulence factor can then be extracted from an experimentally derived Nusselt number by comparing that value with a computed value at the same Reynolds number.

A heat transfer Nusselt number Nu_h was derived from the initial temperature rise of a collector exposed to the combustion gases of the burner. The test conditions were typical of the deposition runs except that distilled water was sprayed into the combustor instead of a salt solution and the collector was not internally cooled. The relationship between the initial slope of the heating curve of the collector and Nu_h was derived as follows:

$$Nu_h = \frac{h_{\text{mix}} L}{\lambda_{\text{mix}}} \quad (18)$$

where

$$h_{\text{mix}} = \frac{\dot{Q}}{A_t (T_{\infty} - T_w)_h} \quad (19)$$

and

$$\dot{Q} = m_t c_{p,t} \frac{d(\text{millivolt})}{dt} \frac{dT}{d(\text{millivolt})} \quad (20)$$

$$\frac{d(\text{millivolt})}{dt} \quad \text{initial rate of increase in millivolt output of thermocouple}$$

$$\frac{dT}{d(\text{millivolt})} \quad \text{slope of temperature-electromotive force function for thermocouple}$$

Then substituting equations (19) and (20) into equation (18) gives

$$Nu_h = \frac{m_t c_{p,t} L}{\lambda_{\text{mix}} A_t (T_{\infty} - T_w)_h} \frac{d(\text{millivolt})}{dt} \frac{dT}{d(\text{millivolt})} \quad (21)$$

The values of all parameters in equation (21) are known or preset except T_w and $d(\text{millivolt})/dt$, which can readily be measured. The term Nu_h in equation (21) implicitly contains F_{turb} because main-stream turbulence affected the heat transfer to the collector. The main-stream turbulence effect can be extracted from Nu_h by comparing its value to the computed value at the same Reynolds number. Thus

$$Nu_{h,\text{comp}} = (0.4 \text{ Re}^{1/2} + 0.06 \text{ Re}^{2/3}) \text{Pr}^{0.4} \left(\frac{T_0}{T_w} \right)^{-0.04} \quad (22)$$

Equation (22) is the relationship between the Nusselt number and the Reynolds number used in the CFBL theory (ref. 44). Because $Nu_{h,\text{comp}}$ does not contain the main-stream turbulence effect, the two Nusselt numbers can be related through F_{turb} ,

$$F_{\text{turb}} Nu_{h,\text{comp}} = Nu_h \quad (23)$$

For equation (21) to be applicable, the collector must have sufficient thermal conductivity to prevent a temperature gradient across the wall thickness. Thus a gold-plated copper collector was fabricated with the same dimensions as the Pt-20% Rh collectors used in the deposition experiments. The gold plating was applied to protect the copper from oxidation. Unfortunately the plating did not survive the initial runs and thus the data obtained from these experiments are considered preliminary. Future calorimetry tests will be conducted with silver collectors. The time for the first 2-mV increase in the thermocouple output from the copper data presently available was used in equation (21) and yielded an Nu_h of 60.94. The heat transfer Nusselt number $Nu_{h,\text{comp}}$ computed with equation (22) was 58.78. Thus using equation (23) gave

$$F_{\text{turb}} = \frac{60.94}{58.78} = 1.04$$

When the calorimetry data were corrected for heat transfer by radiation, estimated to be about 4 percent, the turbulence factor came to about 1. Thus $F_{\text{turb}} = 1$ was assigned to the CFBL computer code when it was used to compute the deposition rates presented in figures 19, 20, 23, 24, 25, and 26.

Discussion

Three modes of deposition have been identified in the literature (refs. 52 and 53) and are characterized in (ref. 9) and reproduced here in table IV. The first mode is vapor diffusion, the mode initially assumed to be primarily applicable in these burner rig tests. The other two deposition modes are particle diffusion and inertial impaction. Particle diffusion included such processes as Brownian diffusion, eddy diffusion, and thermophoresis (thermal diffusion of heavy molecule-size particles across a temperature gradient). Particle impaction is an ever present possibility in high-velocity gas systems whenever macroscopic particles can enter into the gas stream (e.g., carbonaceous particles from a poorly designed or operated combustor). In practice these three very distinct modes of deposition need not be exclusive nor entirely independent even if one mode may predominate. Thus the gas stream may consist of vapors of condensible species and of particles such that deposition may result from a combination of vapor diffusion and, say, eddy impaction, as is thought to occur on turbine components in marine gas turbine engines (ref. 6). Inertial effects may also change the local mass loading of particles at the outer edge of the Brownian diffusion sublayer and alter its diffusional deposition rate (ref. 9).

Examples of deposition modes cited in the literature, occurring in service or in service-simulating rigs, include the work of Jackson (ref. 54), who used an air-cooled probe to study deposit formation in residual-fuel-oil-fired boilers. Jackson concluded that the dominant mode of deposition was vapor diffusion of NaOH or Na₂SO₄ across the boundary layer. Stevens and Tidy (ref. 7), using an industrial gas turbine simulator, concluded that deposition occurred through vapor mass transfer of NaOH or NaCl across the boundary layer. These species were assumed to be converted to Na₂SO₄ within the boundary layer. The Na₂SO₄ then condensed as its surface concentration reached the saturation vapor pressure. Their values of threshold sodium concentration in the fuel at which deposition occurred in their rig compared favorably with those values in land-based gas turbines only when other elements such as Ca, Mg, or K were added in the fuel to the rig.

Using an industrial gas turbine simulator, Vermes (ref. 55) concluded that the fifteenfold increase in deposition rate in a cooled cascade as compared with the case of an adiabatic cascade can be attributed to thermophoresis versus eddy diffusion modes of deposition for the two cases, respectively.

The CFBL theory is capable of handling vapor and heavy-molecule deposition modes (top two rows in table IV), which covers the service type of examples just discussed. Thus, in contrast to previous treatments of vapor deposition (refs. 56 and 57), the CFBL theory

makes explicit provision for the effects of (1) element transport by species of differing mobility, (2) thermal (Soret) diffusion, (3) free-stream turbulence intensity and scale, and (4) variable gas properties across the gaseous boundary layer. Figure 33 illustrates the effect on deposition when multicomponent transport (item (1) above) occurs, as compared with the more simplified approach of considering only Na₂SO₄(g) diffusion through the boundary layer. The parameters listed in figure 33 are those used in appendix C, an example CFBL calculation, where T_0 was 1736 K. At this temperature a consideration of all pertinent sodium species provided about a 24-percent increase in deposition rate when Soret diffusion was also included (item (2) above) and about a 40-percent increase without Soret diffusion when compared with the single-component diffusion of Na₂SO₄. According to figure 33, at $T_0 = 1736$ K, Na₂SO₄ deposition occurred primarily through transport of NaOH(g) and Na(g), but not Na₂SO₄(g). In fact, the Na₂SO₄ species can contribute to a net loss of the Na₂SO₄ condensate layer because of a negative concentration gradient for this species across the boundary layer, i.e., when the vapor pressure of Na₂SO₄ above the Na₂SO₄ condensate exceeds the partial pressure of Na₂SO₄ at the outer edge of the boundary layer.

In the CFBL framework, gas-phase conversion of NaCl to Na₂SO₄ in the available residence time is not necessary for the process of Na₂SO₄ deposition. Of more importance are such heterogeneous reactions at the gas-condensate interface that convert the sodium species (NaOH(g), NaCl(g), and Na(g)) to the Na₂SO₄(c) in the presence of excess oxygen- and sulfur-containing vapor species and the ability to treat solution condensates, which probably exist in deposits on turbine components in many service applications.

Figures 19, 20, and 23 to 26 compare the experimentally determined deposition rates for burner rig tests

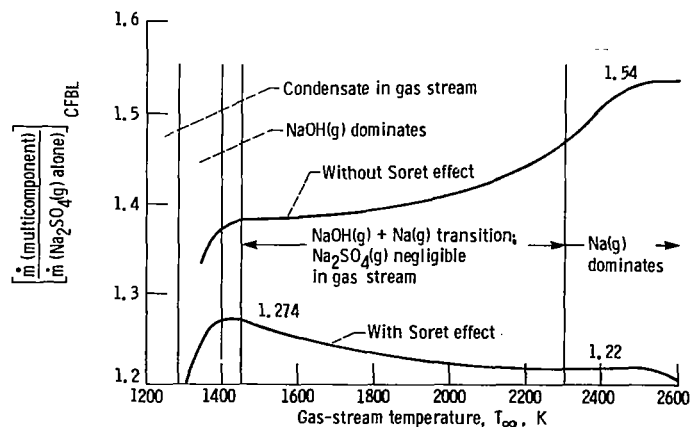


Figure 33. — Multicomponent effect of CFBL theory on deposition rate of Na₂SO₄ as a function of gas-stream temperature. Collector temperature, T_w , 627° C; ambient pressure, p_∞ , 1 atm; fuel-to-air ratio, f , 0.0481; Na₂SO₄ seed, 19 ppm.

that were seeded with Na_2SO_4 , synthetic sea salt, K_2SO_4 (ambient and preheated combustion air), NaCl , and NaNO_3 , respectively, with the predicted values from the CFBL program. Table II lists the percentage differences for the calculated plateau deposition rates with respect to the experimental values. The excellent agreement obtained with NaCl is contrasted by the poor agreement with Na_2SO_4 and the fair agreement provided with the other salts. If the experimental data from the salt runs were about the same factor higher or lower than the predicted values, systematic errors might be suspected in the estimates of the free-stream turbulence factor F_{turb} or the mass transfer Nusselt numbers $\text{Nu}_{m,i}$. (Although $\text{Nu}_{m,i}$ are specific for each alkali metal vapor species, all values of the species of concern here are within the same order of magnitude.) However, a consistently high or low deviation from the predicted deposition rates is not the case, so other sources must be considered to account for the disagreement. All of the other factors in equation (1), except concentration gradient, provide for this application only a minor contribution to the fluxes (i.e., within the scatter of the data). In regard to the concentration gradient, thermodynamic equilibrium was assumed at the gas boundary layer and the boundary layer wall interfaces. Unequal deviations, in the proper direction, from the equilibrium assumption for different seeded salts could provide better agreement with the experimental data. But a nonequilibrium system is not tractable for calculation purposes until some modeling of the kinetics of sulfur- and alkali-metal-containing hydrocarbon flames becomes available. Of course, direct measurements of the sulfur and alkali species of the combustion gases would be helpful.

At this point in the investigation it is premature to assume that adjustments in the vapor diffusion equation are necessary to obtain better agreement between theory and experiment. It is quite possible that vapor diffusion is not the only mode operable in these burner rig tests. As discussed above, the various modes of deposition are not exclusive and the establishment of one mode, even if predominant, does not preclude a contribution to the total deposition by another mode. Evidence has been presented that suggests Na_2SO_4 droplets can survive their residence in the combustor. If these droplets are sufficiently large, they may deposit by inertial impaction. As an upper limit, all droplets within the projected area of the target (if they all stuck) would contribute to the deposit. The deposition rate could then be as much as a factor $\text{Re}^{1/2}$ greater than that by vapor diffusion (ref. 41), where Re is the Reynolds number. In this case the factor can be as much as two orders of magnitude.

The problem now is to use the measured droplet size distribution of the atomized Na_2SO_4 solution and first determine its reduced droplet diameter due to vaporization in the combustor and then determine if

these smaller droplets are sufficiently large to inertially impact. This can be done by comparing the calculated Stokes number, corrected for non-Stokesian drag and gas-stream compressibility, with the critical Stokes number. If the calculated value is larger than the critical value, the deposition rate by inertial impaction can then be calculated by using the proper collection efficiency from the literature. These calculations are presented in appendix E for the Na_2SO_4 case whose droplet size distribution is known, and only the results are given here. The residence time in the combustor was determined during these calculations, and the value is more precise than that determined by the simple calculation given in the section Salt Spray Size Distribution and Droplet Survival. Thus in appendix E consideration is given to the acceleration of the droplet from zero to the main-stream velocity and yields a total residence time of 2.7 msec as compared with the 2.3 msec from the simple calculation.

From appendix E it is seen that sufficiently large droplets of Na_2SO_4 can survive the combustor to inertially impact. The deposition flux was calculated to be

$$\dot{m}'' = (278.8)\eta, \text{ mg/cm}^2\text{hr} \quad (24)$$

and a deposition rate of

$$\dot{m} = (674.5)\eta, \text{ mg/hr} \quad (25)$$

where

η capture efficiency of collector

The capture efficiency was determined graphically to be between 0.03 and 0.05, yielding a deposition rate from equation (25) of 23.3 to 38.2 mg/hr. The experimentally determined plateau value for the deposition rate of the Na_2SO_4 -seeded combustor was 26.9 ± 2.7 mg/hr (table II and fig. 19), which is encompassed by the values predicted from the inertial impaction calculations.

The evidence for an inertial impaction mode of deposition for the Na_2SO_4 -seeded experiments is summarized as follows:

(1) The experimentally determined plateau deposition rates exceeded those predicted from the CFBL theory. Inertial impaction is a more efficient mode of deposition than vapor diffusion through the boundary layer.

(2) Calculations based on droplet size measurements indicate that Na_2SO_4 droplets survived their residence in the combustor. (See the section Salt Spray Size Distribution and Droplet Survival.)

(3) In the stationary collector runs the amount of deposit on the collector surface facing upstream was much greater than that on the surface facing downstream. This amount should not have been more than 70 percent if the mode of the deposition was vapor diffusion with the

temperature profile around the collector within the plateau regime of the deposition rate curve. (See the section Salt Distribution—No Rotation.)

(4) The rate of deposition measured in the plateau region agreed with that calculated from inertial impaction (appendix E).

As mentioned earlier, the salt solution concentration normally used in corrosion tests in the Mach 0.3 burner rigs at Lewis (and the previous deposition tests, ref. 36) was approximately doubled to reduce run time. Also, atomizing air gage pressure for the salt injector, which is normally set at 280 kPa (40 psi), had been reduced to 34 kPa (5 psi). These changes in test parameters are believed to have influenced the deposition mode in the present study. From the droplet size distribution of Na_2SO_4 solution air atomized at gage pressures of 210 kPa (30 psi) (the highest pressure tested), the SMD was found to be 14.5 μm , as compared with 24.6 μm at 34 kPa (5 psi). Calculations like those presented in the section Salt Spray Size Distribution and Droplet Survival using the SMD value at 210-kPa (30-psi) atomizing air gage pressure gave a time for complete vaporization of 3.4 msec. When the concentration of the Na_2SO_4 solution was reduced by a half, assuming the size distribution remained the same, the time for complete vaporization was reduced further to 3.0 msec, which would be close to the residence time of these droplets in the combustor. These calculations suggest that vapor diffusion was a dominant, but not necessarily exclusive, mode in the previous corrosion and deposition work done at this laboratory. In fact, the CFBL-predicted values for the deposition rate of Na_2SO_4 -seeded runs in reference 36 agreed with the experimental values at temperatures well below the dewpoint, as stated earlier (fig. 3). Important is the revelation that the test parameters of these Mach 0.3 burner rigs, such as solution concentration, atomizing air pressure, and solution flow rate (salt pump speed), can be adjusted so as to alter the deposition mode of the Na_2SO_4 -seeded experiments and perhaps for the other salts as well. Tests to explore these possibilities are now being formulated.

Except for the data above the melting point of Na_2SO_4 (884° C), the experimental deposition rates for NaCl-seeded runs are in good agreement with the CFBL-predicted rates. This result suggests that in the NaCl case deposition was indeed by vapor diffusion. The fact that the analysis of the deposit detected only the presence of Na_2SO_4 and no chloride (the section NaCl and NaNO_3 Results) further supports vapor deposition because it cannot be assumed that inertially impacted NaCl droplets converted to Na_2SO_4 while on the collector surface during the 30-minute run duration. The recent work of Fielder et al. (ref. 58) indicates that NaCl crystals take hours, not minutes, to convert to Na_2SO_4 at 800° C. Thus, it is believed that the higher vapor pressure of NaCl

permits the complete vaporization of these solution droplets during their residence in the combustor under the conditions of these tests.

By comparing the deposition rate data of the remaining salts studied herein with their CFBL-predicted rates, it would seem that the principal (but not exclusive) mode of deposition was vapor diffusion (figs. 20, 23, 24, and 26). However, the lack of droplet size data for these salt solutions precludes a more extensive analysis at this time.

It must be emphasized that even with the best of agreement between theory and experiment on the deposition of an Na_2SO_4 layer, there still remains the challenging problem of correlating the amount of deposit with the extent of corrosion. The latter appears to be very sensitive to alloy composition and to salt concentration in the combustion gases, as can be seen in references 59 and 60. Furthermore the dependence of corrosion on salt concentration was not linear with the relatively high salt concentrations reported in these references, up to 6 ppm Na by weight (as NaCl) in reference 59 and 10 ppmw sea salt in reference 60. Both concentrations are with respect to the combustion gases. With some alloys the corrosion rate actually decreased at the higher salt concentrations. With U-700 (a nickel-base superalloy) the corrosion rate as determined by an inductance technique displayed an S-shaped relationship with relatively low concentrations, <1 ppmw Na as NaCl (ref. 61). In reference 62 the corrosion rate of a nickel-base superalloy was determined as a function of Na_2SO_4 thickness (10^{-4} to 0.3 cm) in two different environments, pure oxygen and a simulated gas turbine combustion gas environment consisting of $\text{O}_2 + 0.15$ percent SO_2 . The specimens were exposed at 896° C for 24 hours in both environments. In pure O_2 the corrosion rate was linear with the logarithm of the salt thickness, but it reached a maximum in the simulated gas turbine environment. Thus there does not seem to be a simple relationship between salt concentration or the amount of salt deposit and the extent of the corrosion that occurs. Nevertheless, we are confident that quantitative knowledge of the deposition rates and liquid layer dynamics (ref. 63) will eventually prove valuable in understanding the total corrosion process, in finding methods to eliminate or reduce hot corrosion attack, and certainly in studying the problem of fouling, where correlations with corrosion rates are not required.

Concluding Remarks

The modified Mach 0.3 burner rig and experimental procedures employed in this study have been sufficient to provide data for a reliable comparison with the chemically frozen boundary layer (CFBL) theory of deposition. The analysis of the data shows that under the conditions of these tests, Na_2SO_4 -seeded deposition

occurred primarily by inertial impaction of droplets that did not have enough time to evaporate, but that the test parameters can be altered to change the deposition mode to essentially that of vapor diffusion. Seeding the combustor with NaCl results in the deposition of Na_2SO_4 only and the mode appears to be essentially vapor diffusion. That only Na_2SO_4 was found in the deposit indicates complete conversion of the chloride to the sulfate despite the brief residence time of the reactant in the combustor. The modes of deposition for runs seeded with K_2SO_4 and NaNO_3 have not been studied as extensively as for Na_2SO_4 , but vapor diffusion appears to be the predominant, though not exclusive, mode. Synthetic sea salt is mostly NaCl and its mode of depositing Na_2SO_4 should be similar to that for NaCl, except for the complication that small amounts of other compounds will also deposit, like MgO and CaSO_4 .

No effort has been made herein to relate the amount or composition of the deposits to the degree of corrosion these contaminants will cause on gas turbine alloys, but

the results of this study provide a better understanding of the deposition process associated with these Mach 0.3 burner rigs and will contribute to more precise interpretation of the hot corrosion data generated from these and similar rigs.

This ability suggests hot corrosion mechanistic studies that have been conducted in furnaces may in the near future be conducted in Mach 0.3 burner rigs with the equivalent control of the pertinent parameters and the same confidence in the interpretation of the results, but with the added feature of including the effects of dynamic forces on the mechanism. The burner rig, then, will be able to provide a more realistic but tractable approach to hot corrosion mechanistic studies than furnaces can.

National Aeronautics and Space Administration
Lewis Research Center
Cleveland, Ohio, August 15, 1983

Appendix A Symbols

A	area	T	absolute temperature
A_{proj}	projected area of collector	t	time
B	dimensionless transfer parameter	t_r	residence time of droplet inside combustor
c_p	specific heat at constant pressure	$t_{0.9}$	time required for droplet to reach 90 percent of combustion gas velocity
D	Fick (Brownian) diffusion coefficient	U	velocity
d	diameter	V	volume
E	error value (goodness of fit)	\dot{W}	mass flow rate
F_d	drag force on droplet	w	Rosin-Rammler parameter characteristic of width of distribution
F_{nep}	correction for variable (nonconstant) properties within boundary layer	x	distance
F_{Soret}	correction factor for thermal diffusion	Y	mole fraction
F_{turb}	correction factor for main-stream turbulence	γ	ratio of heat capacities
f	fuel-to-air ratio by mass	ϵ/k	energy well depth parameter
f_d	drag coefficient	η	capture efficiency of collector
h	heat transfer coefficient	Λ	latent heat of vaporization (sublimation)
j''	diffusion mass flux	λ	thermal conductivity
L	characteristic target dimension	μ	viscosity
Le	Lewis number	ρ	density
l	distance from salt injector to nozzle throat	σ	intermolecular potential size parameter
M	molecular weight	τ	characteristic particle acceleration time
Ma	Mach number	Ω	collision integral
m	mass	ω	mass fraction in gas mixture
\dot{m}	mass deposition rate	Subscripts:	
\dot{m}''	deposition mass flux	c	gas stream inside combustor
$\dot{m}''(0)$	plateau deposition mass flux	comp	computed
N	concentration of Na_2SO_4 in water	D	diffusion coefficient
Nu	Nusselt number	dp	dewpoint
P	Rosin-Rammler size distribution density function by weight fraction	f	final
PE	Rosin-Rammler parameter characteristic of height of distribution	h	heat transfer
Pr	Prandtl number	i	species
p	pressure	in	initial conditions
p_{vap}	vapor pressure	j	jet nozzle
\dot{Q}	heat transfer rate	m	mass transfer
q	any test or property parameter	mix	combustion gas mixture
R	universal gas constant	p	molten Na_2SO_4 droplet
Re	Reynolds number	s	Na_2SO_4 solution droplet
S	cross-sectional area of combustor liner	T	thermal diffusion (thermophoresis)
S_q	ratio of fractional change in deposition rate to fractional change in q	t	collector
Sc	Schmidt number	w	gas side of interface (wall)
Stk	Stokes number	0	stagnation conditions
Stk_{eff}	Stokes number corrected for non-Stokesian drag (effective Stokes number)	μ	viscosity
$\text{Stk}_{\text{eff},\text{Ma}}$	effective Stokes number corrected for compressibility effects	∞	gas stream outside of combustor unaffected by collector

Appendix B

Derivation of an Empirical Deposition Equation

The premise of the derivation is that for each species

$$-\dot{m}_i'' \propto p_{i,\infty} - p_{i,w} \quad (\text{B1})$$

where $p_{i,\infty}$ is the gas-stream partial pressure of the species, $p_{i,w}$ is its partial pressure at the wall, and \dot{m}_i'' is its deposition flux. Note that $p_{i,w}$ is assumed to be an equilibrium pressure (i.e., $p_{i,w}$ is also the vapor pressure p_{vap} of the species at the wall temperature).

At a wall temperature T_w the mass flux becomes

$$-\dot{m}_i''(T_w) \propto [p_{i,\infty} - p_{\text{vap},i}(T_w)] \quad (\text{B2})$$

where () represents the functional dependence.

When the temperature of the wall is the dewpoint temperature T_{dp} , mass flux becomes zero and the vapor pressure of the species at the wall becomes equal to the partial pressure of the species in the gas stream, that is, when $T_w = T_{\text{dp}}$,

$$-\dot{m}_i''(T_{\text{dp}}) = 0$$

and

$$p_{i,\infty} = p_{\text{vap},i}(T_{\text{dp}}) \quad (\text{B3})$$

Note that $p_{i,\infty}$ is constant (independent of T_w) and defines the dewpoint temperature through equation (B3).

Far below the dewpoint the vapor pressure of the species at the wall is much less than the partial pressure of the species in the gas. Thus

$$p_{\text{vap},i}(T_w) < p_{i,\infty} \quad \text{at } T_w < T_{\text{dp}} \quad (\text{B4})$$

and

$$-\dot{m}_i''(0) \propto p_{i,\infty} \quad \text{at } T_w < T_{\text{dp}} \quad (\text{B5})$$

where $\dot{m}_i''(0)$ is defined as that deposition flux that is constant with respect to wall temperature and depends only on the gas-stream partial pressure of the species.

Assuming the proportionality constants associated with expressions (B2) and (B5) to be independent of temperature, the following equations result from taking the ratio of equations (B2) and (B5):

$$\frac{-\dot{m}_i''(T_w)}{-\dot{m}_i''(0)} = 1 - \frac{p_{\text{vap},i}(T_w)}{p_{i,\infty}} \quad (\text{B6})$$

where the equality symbol was added after the constants of proportionality were cancelled out.

The temperature dependence of the vapor pressure is given by the Clausius-Clapeyron equation

$$\frac{dp_{\text{vap},i}}{dT} = \frac{\Lambda}{RT^2} p_{\text{vap},i} \quad (\text{B7})$$

where

Λ latent heat of vaporization

R universal gas constant

Then

$$\int_{p_{\text{vap},i}(T_{\text{dp}})}^{p_{\text{vap},i}(T_w)} \frac{dp_{\text{vap},i}}{p_{\text{vap},i}} = \int_{T_{\text{dp}}}^{T_w} \frac{\Lambda}{RT^2} dT \quad (\text{B8})$$

$$\frac{p_{\text{vap},i}(T_w)}{p_{\text{vap},i}(T_{\text{dp}})} = \exp \left[-\frac{\Lambda}{RT_{\text{dp}}} \left(\frac{T_{\text{dp}}}{T_w} - 1 \right) \right] \quad (\text{B9})$$

But $p_{i,\infty} = p_{\text{vap},i}(T_{\text{dp}})$ from equation (B3); thus

$$\frac{p_{\text{vap},i}(T_w)}{p_{i,\infty}} = \exp \left[-\frac{\Lambda}{RT_{\text{dp}}} \left(\frac{T_{\text{dp}}}{T_w} - 1 \right) \right] \quad (\text{B10})$$

Substituting equation (B10) into equation (B6) gives the desired relationship

$$\frac{-\dot{m}_i''(T_w)}{-\dot{m}_i''(0)} = 1 - \exp \left[-\frac{\Lambda}{RT_{\text{dp}}} \left(\frac{T_{\text{dp}}}{T_w} - 1 \right) \right] \quad (\text{B11})$$

Equation (B11) was tested by Rosner and Atkins (ref. 42), who applied it to their K_2SO_4 deposition rate data accumulated by laser optics. They found good agreement between their experimental data and this simple vapor equation.

Appendix C

Simplified Example Calculation Using CFBL Theory

The diffusion mass flux of each species is given in the main text (eq. (1)) and repeated here:

$$-j''_{i,w} = \left[F_{\text{turb}} \frac{(D_i \rho)_{\infty}}{L} F_{i,\text{Soret}} \text{Nu}_{m,i} \right] \times \left[(\omega_{i,\infty} - \omega_{i,w}) - B_{T,i} \frac{F_{\text{nep}}}{F_{i,\text{Soret}}} \omega_{i,w} \right] \quad (\text{C1})$$

If thermal diffusion effects and free-stream turbulence are neglected, equation (C1) simplifies to

$$-j''_{i,w} = \frac{(D_i \rho)_{\infty}}{L} \text{Nu}_{m,i} (\omega_{i,\infty} - \omega_{i,w}) \quad (\text{C2})$$

The simplified version of the theory will be used to illustrate a calculation of the deposition rates for the Na_2SO_4 -seeded run for which data were presented in figure 19 and table II. Some of the steps in the procedures are not as rigorous as their counterparts in the CFBL computer program but lend themselves more readily to hand calculation. The procedure adopts the stepwise format of Helt (ref. 64), who attempted to apply the concepts of Rosner et al. (refs. 36 to 41), to the flue gases of a fluidized-coal-bed combustor with a 2.54-cm (1-in.) long target maintained at 1000 K in a particular 10-atm, 1200 K stream. Unfortunately Helt appears to have erroneously interpreted, evaluated, and used the relevant gas mixture density, Reynolds number, and mixture heat diffusivity (entering the Soret effect correction factors). Moreover, rather than imposing strict local thermochemical equilibrium at the vapor-condensate interface subject to Na/S element flux ratio constraint, Helt has for simplicity arbitrarily set $\omega_{i,w} = 10^{-2} \omega_{i,e}$ for each of the dominant Na-containing species (NaCl , Na_2SO_4 , etc.). Nevertheless, Helt has spelled out many of the essential features of the CFBL theory.

The steps are

- (1) Assign values to T_0 , T_w , p_0 , p_{∞} , f , and L .
- (2) Calculate T_{∞} , M_{mix} , and $D_{i,\text{mix}}$
- (3) Calculate Re , Sc_i , and $\text{Nu}_{m,i}$.

The calculation of the dimensionless transport numbers requires computing ρ_{mix} , $U_{\text{mix},\infty}$, and μ_{mix} .

- (4) From the NASA CEC Code (ref. 45), set $\omega_{i,\infty}$ and $\omega_{i,w}$.
- (5) Calculate the individual fluxes, j''_w .
- (6) Calculate the total diffusional flux of the element sodium

$$-j''_{\text{Na},w} = \sum_i \omega_{\text{Na}/i} j''_{i,w} \quad (\text{C3})$$

(7) Calculate the mass flux of condensed Na_2SO_4 at the wall of the collector

$$-\dot{m}''(\text{Na}_2\text{SO}_4) = \frac{-j''_{\text{Na},w}}{\omega_{\text{Na}/\text{Na}_2\text{SO}_4}} \quad (\text{C4})$$

Using this procedure the computation for the Na_2SO_4 -seeded run is as follows:

Step 1:

$$T_0 = 1736 \text{ K}$$

$$T_w = 900 \text{ K}$$

$$p_0 = 1.07 \text{ atm}$$

$$p_{\infty} = 1 \text{ atm}$$

$$f = 0.048 \quad (\dot{W}_{\text{air}} = 20.02 \text{ g/sec})$$

$$L = 1.91 \text{ cm}$$

Step 2:

$$\frac{p_0}{p_{\infty}} \cong \left(\frac{T_0}{T_{\infty}} \right)^{\gamma/(\gamma-1)} \quad (\text{C5})$$

$$T_{\infty} \cong T_0 \left(\frac{p_{\infty}}{p_0} \right)^{(\gamma-1)/\gamma} = 1713 \text{ K} \quad (\text{C6})$$

where $\gamma = 1.26$ from the NASA CEC code. Equations (C5) and (C6) apply only for isentropic conditions, which are not applicable to a burner rig exhausting into the atmosphere. We chose to use these equations, however, to derive an estimate of T_{∞} as there is no precise way of determining its value. Fortunately, this estimation introduces only a small error in the subsequent calculations.

$$M_{\text{mix}} = \sum Y_i M_i = 28.800 \text{ g/mole} \quad (\text{C7})$$

also from the NASA CEC code. From the Chapman-Enskog kinetic theory (ref. 65)

$$D_{i,\text{mix},\infty} = \frac{1.858 \times 10^{-3} \left[T_{\infty}^3 \left(\frac{1}{M_i} + \frac{1}{M_{\text{mix}}} \right) \right]^{1/2}}{p_{\infty} \sigma_{i,\text{mix}}^2 \Omega_{D,i,\text{mix}}} \quad (\text{C8})$$

where D is in cm^2/sec when T is in K, p is in atm, and σ is in Å.

The Lennard-Jones parameters listed in references 38 and 66 can be used to estimate σ and ϵ/k ; thus

$$\sigma_{i,\text{mix}}^2 = \left(\frac{\sigma_i + \sigma_{\text{mix}}}{2} \right)^2 \quad (\text{C9})$$

$$\left(\frac{\epsilon}{k} \right)_{i,\text{mix}} = \sqrt{\left(\frac{\epsilon}{k} \right)_i \left(\frac{\epsilon}{k} \right)_{\text{mix}}} \quad (\text{C10})$$

and $\Omega_{D,i,\text{mix}}$ can be determined from table B-2 in reference 65 for the computed values of $T_{\infty}/(\epsilon/k)_{i,\text{mix}}$. Table V lists the calculated values of $D_{i,\text{mix}}$ (eq. (C8)) for each of the gaseous species involved. As an example, consider the NaOH species in the combustion gases (essentially air):

$$\begin{aligned} \sigma_{\text{NaOH},\text{air}}^2 &= \left(\frac{\sigma_{\text{NaOH}} + \sigma_{\text{air}}}{2} \right)^2 = \left(\frac{3.804 + 3.617}{2} \right)^2 \\ &= 13.768 \text{ Å}^2 = 0.13768 \text{ nm}^2 \end{aligned}$$

$$\begin{aligned} \left(\frac{\epsilon}{k} \right)_{\text{NaOH},\text{air}} &= \sqrt{\left(\frac{\epsilon}{k} \right)_{\text{NaOH}} \left(\frac{\epsilon}{k} \right)_{\text{air}}} \\ &= \sqrt{(1962)(97.0)} = 436.2 \text{ K} \end{aligned}$$

$$\left(\frac{kT_{\infty}}{\epsilon} \right)_{\text{NaOH},\text{air},\infty} = \frac{1713}{436.2} = 3.927$$

The corresponding $\Omega_{D,\text{NaOH},\text{air},\infty} = 0.8874$

And

$$D_{\text{NaOH},\text{air},\infty} =$$

$$\frac{1.858 \times 10^{-3} \sqrt{(1713)^3 \left(\frac{1}{40.01} + \frac{1}{28.800} \right)}}{(1)(13.768)(0.887)}$$

$$D_{\text{NaOH},\text{air},\infty} = 2.635 \text{ cm}^2/\text{sec}$$

Step 3:

$$\rho_{\text{mix},\infty} = \frac{p_{\infty} M_{\text{mix}}}{RT_{\infty}} = 2.050 \times 10^{-4} \text{ g/cm}^3 \quad (\text{C11})$$

$$U_{\text{mix},\infty} = \frac{RT_{\infty}}{p_{\infty} M_{\text{mix}}} \frac{\dot{W}_{\text{mix}}}{A_j} \quad (\text{C12})$$

$$\dot{W}_{\text{mix}} = \dot{W}_{\text{air}}(1+f) = 20.98 \text{ g/sec} \quad (\text{C13})$$

The atomizing air through the salt injector was not included in the mass flow calculation.

Next we calculate the effective area, which is a function of the discharge coefficient of the exit nozzle. For the purpose of this example calculation, the discharge coefficient is taken as unity and the area is taken as the geometrical area of the throat of the nozzle, that is,

$$A_j = \frac{\pi d_j^2}{4} = 5.067 \text{ cm}^2 \quad (\text{C14})$$

where the exit nozzle diameter d_j is 2.54 cm. Then from equation (C12)

$$U_{\text{mix},\infty} = 2.02 \times 10^4 \text{ cm/sec}$$

The viscosity can be computed from the low-density Chapman-Enskog theory equation (ref. 65)

$$\begin{aligned} \mu_{\text{mix},\infty} &= 2.669 \times 10^{-5} \sqrt{\frac{M_{\text{mix}} T_{\infty}}{\sigma_{\text{air}}^2 \Omega_{\mu,\text{air},\infty}}} \text{ g/cm-sec} \\ &\quad (\text{when } T \text{ is in K and } \sigma \text{ is in Å}) \quad (\text{C15}) \end{aligned}$$

where the viscosity is insensitive to pressure. The Lennard-Jones parameters for air are listed in table V and Ω_{μ} can be interpolated from table B-2 in reference 65. In this example $\Omega_{\mu,\text{air},\infty} = 0.76$ and $\mu_{\text{mix},\infty} = 5.95 \times 10^{-4} \text{ g/cm-sec}$.

Now all the information is available for calculating the dimensionless numbers.

$$Re = \frac{L U_{mix,\infty} \rho_{mix,\infty}}{\mu_{mix,\infty}} \quad (C16)$$

$$Sc_i = \frac{\mu_{mix,\infty}}{\rho_{mix,\infty} D_{i,mix,\infty}} \quad (C17)$$

$$Nu_{m,i} = (0.4 Re^{1/2} + 0.06 Re^{2/3}) Sc_i^{0.4} \left(\frac{T_0}{T_w} \right)^{-0.04} \quad (C18)$$

The values for Re , Sc_i , and $Nu_{m,i}$ are listed in table VI.

Step 4:

The mass fraction of each species at the outer side and the wall side of the boundary layer is obtained from the NASA CEC code and is listed in table VI. The composition of the sodium species at the wall of the collector was not adjusted for the effect of element segregation associated with different Fick diffusivities of the components in the boundary layer (i.e., the Na/S ratio at the wall was taken to be the same as that in the main stream). Under the conditions of these experiments the correction for the element segregation is within the scatter of the data (e.g., see table 2.1 of ref. 38 and fig. 3 for the magnitude of the segregation effect and compare that with the scatter of the data in fig. 19). However, element segregation is a feature of the computer code of the CFBL theory (ref. 44) and can be the rationale for dramatic variations from thermodynamically predicted "dewpoint" and condensate composition expectations (ref. 46).

Step 5:

By using equation (C2), the information contained in table VI, and the value for $\rho_{mix,\infty}$, the flux for each species can be computed. These flux values are listed in table VI. Note that the flux of Na_2SO_4 across the boundary layer is small as compared with the flux of the other two sodium species. The dominant source of sodium for the deposition of Na_2SO_4 comes from NaOH.

Step 6:

The total flux of sodium is computed by using equation (C3) and amounts to

$$-j''_{Na,w} = 1.291 \times 10^{-7} \text{ g/cm}^2\text{-sec}$$

Step 7:

The mass flux of Na_2SO_4 condensate on the collector is calculated from equation (C4):

$$-\dot{m}''(Na_2SO_4) = 3.988 \times 10^{-7} \text{ g/cm}^2\text{-sec}$$

and, as the area of the collector is 7.601 cm^2 ,

$$\dot{m}(Na_2SO_4) = 10.9 \text{ mg/hr}$$

The value for the deposition rate of Na_2SO_4 provided from the CFBL computer code at $T_w = 900 \text{ K}$ is 11.7 mg/hr . The 7-percent disparity between the hand-calculated value for \dot{m} and the computer-calculated value is due to the more accurate computational procedures used in the CFBL code and its inclusion of the thermophoretic effects.

Appendix D

Sensitivity Analysis of Theory Parameters

The multicomponent CFBL theory program predicts vapor deposition rates as a function of test parameters for assumed values of various property parameters. Accordingly, if q is any test or property parameter, we can write

$$\dot{m} \propto q^{S_q} \quad (\text{D1})$$

where

\dot{m} deposition rate

The sensitivity value S_q is the ratio of the fractional change in the deposition rate to the fractional change in q . Taking the derivative of equation (D1) gives

$$d\dot{m} \propto S_q q^{S_q-1} dq \quad (\text{D2})$$

and dividing equation (D2) by equation (D1) gives

$$\frac{d\dot{m}}{\dot{m}} = S_q \frac{dq}{q} \quad (\text{D3})$$

where the equality sign is inserted as the proportionality constant is cancelled out. Solving for S_q provides its definition.

$$S_q = \frac{d\dot{m}/\dot{m}}{dq/q} = \frac{d \ln \dot{m}}{d \ln q} \quad (\text{D4})$$

Thus from equation (D3) a 10-percent change in q will provide a $10 S_q$ -percent change in the predicted deposition rate. But S_q must still be evaluated. The procedure employs finite difference approximation. From the Taylor Series

$$\dot{m}(q + \Delta q) \approx \dot{m}(q) + \left(\frac{d\dot{m}}{dq} \right)_q \Delta q + \left(\frac{d^2\dot{m}}{dq^2} \right)_q \frac{\Delta q^2}{2} + \dots (\text{D5})$$

and

$$\dot{m}(q - \Delta q) \approx \dot{m}(q) - \left(\frac{d\dot{m}}{dq} \right)_q \Delta q + \left(\frac{d^2\dot{m}}{dq^2} \right)_q \frac{\Delta q^2}{2} + \dots (\text{D6})$$

Subtracting equation (D6) from equation (D5) gives

$$\dot{m}(q + \Delta q) - \dot{m}(q - \Delta q) = \left(\frac{d\dot{m}}{dq} \right)_q 2 \Delta q \quad (\text{D7})$$

Substituting equation (D7) into equation (D4) yields the solution for S_q :

$$S_q = \frac{d \ln \dot{m}}{d \ln q} = \frac{\dot{m}(q + \Delta q) - \dot{m}(q - \Delta q)}{2 \Delta q} \frac{q}{\dot{m}(q)} \quad (\text{D8})$$

Table VII presents values for S_q that have been calculated by using equation (D8) for the case $\Delta q/q = 0.05$ and at parameter q values near to those used in appendix B. Note that for the seed level, S_q is about unity and thus the deposition rate would be predicted to vary approximately linearly with seed level in this range. This prediction is in agreement with the experimental data presented in figures 12 and 13. With respect to wall temperature, a 10-percent change (± 90 K) produces only a $10 \times 0.0433 = 0.433$ -percent change in the deposition rate. This small change, of course, is due to $T_w = 900$ K being on the deposition rate plateau, where the rate is insensitive to T_w (fig. 19).

Sensitivity values for transport parameters like σ_{NaOH} , the intermolecular potential size parameter for sodium hydroxide, are particularly important as these parameters are estimated quantities for which few direct data exist.

Appendix E

Inertial Impaction Calculations

The capture efficiency of a collector in a low-particle-mass-loading, high-velocity flow is mainly determined by an inertial parameter termed the Stokes number. The Stokes number Stk can be viewed as the ratio of the characteristic stopping time of the particle to the characteristic flow time around the collector. Impaction occurs only for Stokes numbers greater than a critical value Stk_{crit} . The stopping time of the particle is usually computed by applying the Stokes (linear) drag law to a particle initially moving with the free-stream velocity. For the situation here, however, the droplets do not obey a linear drag law (i.e., they are non-Stokesian). Thus an effective Stokes number Stk_{eff} must be computed that is dependent on the Reynolds number based on droplet diameter and free-stream velocity. This Stk_{eff} must further be corrected for the compressibility effect of a nonnegligible free-stream Mach number to produce $Stk_{eff, Ma}$. By using $Stk_{eff, Ma}$ the capture efficiency η can be determined graphically from the literature (ref. 67), and the deposition rate can be computed by using equation (E1):

$$\dot{m} = \omega_{p, \infty} \rho_{mix, \infty} U_{mix, \infty} A_{proj} \eta \quad (E1)$$

For the Na_2SO_4 -seeded burner rig data

$$\dot{m} = (18.7 \times 10^{-6})(2.05 \times 10^{-4})(20.199)(1.27)(1.91) \eta, \quad \text{g/sec} \quad (E2a)$$

$$\dot{m} = 1.828 \times 10^{-4} \eta, \text{ g/sec} \quad (E2b)$$

or

$$\dot{m} = 674.5 \eta, \text{ mg/hr} \quad (E2c)$$

To compute Stk_{eff} , the droplet Reynolds number must be calculated, and this requires knowledge of the droplet diameter. Because the droplet diameter is continuously diminishing as a result of vaporization, an average diameter is used in the calculations. Also, air properties at an average temperature $(T_w + T_\infty)/2$ are used because drag on a droplet is a boundary layer effect, where T_w is the droplet surface temperature that was adjusted in equation (10).

The final droplet size distribution can be obtained by considering the history of the droplets from the time of their injection into the combustor until their arrival at the collector. The first step is to determine the diminution of the droplets while they are accelerating to the combustion

gas velocity. The drag force for a droplet of diameter d_p is

$$F_d = -f_d(U_p - U_{mix, c}) \quad (E3)$$

where the drag coefficient is given by Stokes law

$$f_d = 3\pi\mu_{mix}d_p \quad Re << 1 \quad (E4)$$

A correction factor is required because the Reynolds number for the droplet is not much less than unity. For $Re_p < 1000$ an approximately corrected drag coefficient is (ref. 68),

$$f_d = 3\pi\mu_{mix}d_p(1 + 0.158 Re_p^{2/3}) \quad (E5)$$

This corrected value is suitable for the present calculations, but reference 67 provides a more rigorous treatment.

From Newton's first law

$$m_p \frac{dU_p}{dt} = -f_d(U_p - U_{mix, c}) \quad (E6)$$

Then letting $C = (U_p - U_{mix, c})$, equation (E6) becomes

$$m_p \frac{dC}{dt} = -f_d C \quad (E7)$$

and assuming that at $t=0$, $U_p=0$, integration of equation (E7) yields

$$U_p = U_{mix, c} \left(1 - \exp \frac{-t}{\tau}\right) \quad (E8)$$

where $\tau = m_p / f_d$.

$$\tau = \frac{\rho_p \pi / 6 d_p^3}{3\pi\mu_{mix}d_p(1 + 0.158 Re_p^{2/3})} = \frac{\rho_p d_p^2}{18\mu_{mix}(1 + 0.158 Re_p^{2/3})} \quad (E9)$$

The time $t_{0.9}$ required for the droplet to reach 90 percent of the combustion gas velocity, $U_p/U_{mix, c} = 0.9$, from equation (E8) is

$$t_{0.9} = -[\ln(0.1)]\tau \quad (E10)$$

The Sauter mean diameter SMD of the Na_2SO_4 solution spray is $24.6 \mu\text{m}$. Upon complete vaporization of

the water a Na_2SO_4 molten droplet results with a diameter of $3.25 \mu\text{m}$ (eq. (7)). These diameters are employed as characteristic of the droplet diameter size distribution in these calculations. Assume that, by the time the characteristic solution droplet accelerates to 90 percent of the combustion gas velocity, its diameter decreases to $20 \mu\text{m}$. The average diameter during the acceleration then is

$$\frac{24.6 + 20}{2} = 22.3 \mu\text{m}$$

which gives a droplet Reynolds number of

$$\text{Re}_p = \frac{\rho_{\text{mix}} U_{\text{mix},c} d_p}{\mu_{\text{mix}}} = \frac{(3.60 \times 10^{-4})(4791)(2.23 \times 10^{-3})}{426 \times 10^{-6}} = 9.03 \quad (\text{E11})$$

where ρ_{mix} and μ_{mix} were chosen at the average temperature $(T_w + T_0)/2 = (352 + 1736)/2 = 1044 \text{ K}$ and $U_{\text{mix},c}$ is the gas velocity in the combustor given by

$$U_{\text{mix},c} = \frac{RT_0}{p_0 M_{\text{mix}}} \frac{W_{\text{mix}}}{S} = \frac{(82.05)(1736)}{(1.068)(28.8)} \times \frac{(20.98)}{(20.27)} = 4791 \text{ cm/sec}$$

Then from equation (E9)

$$\tau = \frac{(1)(2.23 \times 10^{-3})^2}{(18)(426 \times 10^{-6})[1 + (0.158)(9.03)^{2/3}]} = 0.385 \text{ msec}$$

and from equation (E10)

$$t_{0.9} = -[\ln(0.1)](0.385) = 0.886 \text{ msec}$$

The time for complete evaporation of the water from the SMD solution droplet, as calculated in the main text, is 2.5 msec. The time for a droplet to vaporize from $d_{p,\text{in}}$ to $d_{p,f}$ is

$$t = \frac{\rho_p c_{p,\text{mix}}}{\lambda_{\text{mix}}} \frac{1}{\ln(1 + B_h)} \frac{d_{p,\text{in}}^2 - d_{p,f}^2}{8} \quad (\text{E12})$$

If Re_p is not small, equation (E12) should read

$$t = \frac{\rho_p c_{p,\text{mix}}}{\lambda_{\text{mix}}} \left(\frac{2}{\text{Nu}_m} \right) \frac{1}{\ln(1 + B_h)} \frac{d_{p,\text{in}}^2 - d_{p,f}^2}{8} \quad (\text{E12a})$$

where Nu_m is the mass transfer Nusselt number. However, we have taken $\text{Nu}_m = 2$, assuming that the droplets are spherical and that the medium is quiescent with respect to the droplets. Although these assumptions are not valid during the period the droplets accelerate from their initial velocity up to the gas-stream velocity, the acceleration is exponential and so the period is short as compared with the total vaporization time. Moreover, under these experimental conditions, the Reynolds number based on the droplet diameter and on the gas-stream velocity relative to the droplet is small (i.e., the modification of the Nusselt number (both for heat and mass transfer) due to the additional convective contribution is small as compared with the quiescent medium condition, $\text{Nu}_m = 2$). Therefore the error introduced by our assumptions is negligible and equation (E12a) can be reduced to equation (E12).

Thus the ratio of two times is

$$\frac{t_1}{t_2} = \frac{(d_{p,\text{in}})_1^2 - (d_{p,f})_1^2}{(d_{p,\text{in}})_2^2 - (d_{p,f})_2^2} \quad (\text{E13})$$

As stated above, a $24.6\text{-}\mu\text{m}$ -diameter solution droplet will have its water completely evaporated in 2.5 msec to yield a Na_2SO_4 particle of diameter $3.25 \mu\text{m}$. Thus from equation (E13)

$$\frac{0.886}{2.5} = \frac{24.6^2 - d_{p,f}^2}{24.6^2 - (3.25)^2} \quad (\text{E14})$$

Here the diameter of the SMD solution droplet upon accelerating to 0.9 V reduces to $d_{p,f} = 19.9 \mu\text{m}$. Thus the starting assumption that the diameter of the droplet would reduce to $20 \mu\text{m}$ by the time it accelerated to 90 percent of the gas-stream velocity is satisfactory. If the estimate had been unsatisfactory, the value determined in equation (E14) would have been used to compute a new estimated average, and the calculations represented in equations (E11) to (E14) would have been repeated iteratively until $d_{p,f}$ appeared to “converge.”

The distance traveled by the characteristic solution droplet during acceleration is computed by integrating equation (E8):

$$x = \int_0^{t_{0.9}} U_p dt = \int_0^{t_{0.9}} U_{\text{mix},c} \left[1 - \exp\left(-\frac{t}{\tau}\right) \right] dt \quad (\text{E15})$$

$$x = U_{\text{mix},c} \left\{ t_{0.9} - \tau \left[1 - \exp \left(\frac{-t_{0.9}}{\tau} \right) \right] \right\} \quad (\text{E16})$$

where

$$\left[1 - \exp \left(\frac{-t_{0.9}}{\tau} \right) \right] = 0.9 \quad (\text{E17})$$

Therefore

$$x = U_{\text{mix},c} (t_{0.9} - 0.9 \tau) \quad (\text{E18})$$

From equation (E18)

$$x = 4791 [0.886 - (0.9)(0.385)] \times 10^{-3} = 2.585 \text{ cm}$$

The distance between the salt solution probe and the exit nozzle throat, which is the total distance the droplet has to travel in the combustor, is 10.8 cm, so the remaining distance is $10.8 - 2.6 = 8.2$ cm. The total residence time of the droplet in the combustor is

$$t_{\text{total}} = 0.886 + \frac{8.2}{(0.95)(4791)} \times 1000 = 2.7 \text{ msec}$$

where it is assumed that in the remaining distance, the droplet has an average velocity of $0.95 U_{\text{mix},c}$.

After the water completely vaporizes, there still remains $2.7 - 2.5 = 0.2$ msec residence time in the combustor for vaporization of the characteristic Na_2SO_4 droplet which reduces its diameter, by equation (E13), to

$$\frac{0.2}{9.6} = \frac{3.25^2 - d_{p,f}^2}{3.25^2 - 0} \quad (\text{E19})$$

and $d_{p,f} = 3.2 \mu\text{m}$, where from the main text it was computed to take 9.6 msec to completely vaporize a $3.25\text{-}\mu\text{m}$ -diameter droplet of Na_2SO_4 . Thus the characteristic diameter of the Na_2SO_4 droplets as they leave the combustor is $3.2 \mu\text{m}$.

The droplet Reynolds numbers is given in equation (E11), but now the gas stream has been accelerated in the throat of the exit nozzle to 20 199 cm/sec. Thus from equation (E11)

$$\text{Re}_p = \frac{(2.0 \times 10^{-4})(20\ 199)(3.2 \times 10^{-4})}{593 \times 10^{-6}} = 2.18$$

The Stokes number is defined as

$$\text{Stk} = \frac{\rho_p d_p^2 U_{\text{mix},\infty}}{18 \mu_{\text{mix},\infty} L} \quad (\text{E20})$$

With the Reynolds number correction due to non-Stokesian drag, Stk_{eff} is

$$\text{Stk}_{\text{eff}} = \frac{\rho_p d_p^2 U_{\text{mix},\infty}}{18 \mu_{\text{mix},\infty} (1 + 0.158 \text{Re}_p^{2/3}) L} \quad (\text{E21})$$

and for this case

$$\text{Stk}_{\text{eff}} =$$

$$\frac{(2.698)(3.2 \times 10^{-4})^2 (20\ 199)}{(18)(5.95 \times 10^{-4}) [1 + (0.158)(2.18)^{2/3}] (1.905)} = 0.217$$

The correction for gas-stream compressibility effects at nonnegligible Mach numbers is (ref. 67).

$$(\text{Stk}_{\text{eff}})_{\text{Ma}} = \text{Stk}_{\text{eff}} \frac{[1 - (5/12)\text{Ma}^2 + \dots]}{[1 + (\gamma - 1)/2\text{Ma}^2 + \dots]^{0.67}} \quad (\text{E22})$$

Thus

$$(\text{Stk}_{\text{eff}})_{\text{Ma}} = (0.217)(0.95) = 0.206$$

and

$$0.206 > \text{Stk}_{\text{crit}} = 0.125$$

Therefore the droplet size is sufficiently large for the droplets to be deposited by inertial impaction. By using the graph in reference 67 and $(\text{Stk}_{\text{eff}})_{\text{Ma}} = 0.206$, η is in the range 0.03 to 0.05. The range is due to the inexactness in reading the graph. Substituting η into equation (E2c) gives $\dot{m} = 20.2$ to 33.7 mg/hr. These values encompass the experimentally determined plateau value for the deposition rate of Na_2SO_4 from a Na_2SO_4 -seeded combustor of 26.9 ± 2.7 mg/hr.

References

- Stringer, J.: Hot Corrosion of High-Temperature Alloys, Annual Review of Material Science, vol. 7, R. A. Huggins, R. H. Bube, and R. W. Roberts, eds., Annual Reviews, Inc., 1977, pp. 477-509.
- Hot Corrosion Problems Associated with Gas Turbines, Am. Soc. Test. Mater. Spec. Tech. Publ. (421), 1967.
- Stringer, J.: Hot Corrosion of High Temperature Alloys. Proceedings of the First Conference on Advanced Materials for Alternative-Fuel-Capable Directly Fired Heat Engines, John W. Fairbanks and John Stringer, eds., CONF-790749, 1979, pp. 331-339.
- Gilder, H.; and Morbioli, R.: Sulphidation Behavior of Nickel- and Cobalt-Based Alloys. High Temperature Alloys for Gas Turbines, D. Coutouradis, et al., eds., Applied Science Publishers Ltd. (London), 1978, pp. 125-146.
- Tschinkel, J. G.: Formation of Sodium Sulfate in Gas Turbine Combustors. Corrosion, vol. 28, no. 5, May 1972, pp. 161-196.
- McCreath, C. G.; and Condé, J. F. G.: A State of the Art Review of Factors Contributing to the Turbine Environment Causing Hot Corrosion of Gas Turbines Operating in a Marine Environment. J. Inst. Energy, vol. 54, no. 421, Dec. 1981, pp. 192-196.
- Stevens, C. G.; and Tidy, D.: The Mechanism of Deposition of Fuel-Derived Sodium in Gas Turbines. J. Inst. Energy, vol. 54, no. 3, Mar. 1981, pp. 3-11.
- Condé, J. F. G.; and McCreath, C. G.: The Control of Hot Corrosion in Marine Gas Turbines. Behavior of High Temperature Alloys in Aggressive Environments, I. Kirman, et al., eds., The Metals Society (London), 1979, pp. 497-512.
- Stearns, Carl A.; Kohl, F. J.; and Rosner, D. E.: Combustion System Processes Leading to Corrosive Deposits. DOE/NASA/2593-27, NASA TM-81752, 1981.
- Barkalow, R. H.; and Pettit, F. S.: Erosion/Hot Corrosion Laboratory Evaluation of Metallic Alloys and Coatings. Proceedings of the First Conference on Advanced Materials for Alternative-Fuel-Capable Directly Fired Heat Engines. John W. Fairbanks and John Stringer, eds., CONF-790749, 1979, pp. 270-286.
- Hancock, P.; and Nicholls, J. R.: Mechanical Aspects of Corrosion Mechanisms in Marine Turbines. Proceedings of the 4th Conference on Gas Turbine Materials in a Marine Environment, vol. I, U.S. Naval Sea Systems Command, 1979, pp. 403-422.
- Hancock, P.: Rig Testing to Study Environmental Effects on Hot Salt Corrosion Mechanism. Proceedings of the 4th Conference on Gas Turbine Materials in a Marine Environment, vol. I, U.S. Naval Sea Systems Command, 1979, pp. 465-474.
- Booth, G. C.; Galsworthy, J. C.; and Taylor, A. F.: Low and High Pressure Rig Testing of Materials and Coatings. Proceedings of the 4th Conference on Gas Turbine Materials in a Marine Environment, vol. I, U.S. Naval Sea Systems Command, 1979, pp. 259-272.
- Restall, J. E.: The Degradation of Hot Components in Gas Turbine Engines. Environmental Degradation of High Temperature Materials, vol. 1, Spring Residential Conference, series 3, no. 13, Institution of Metallurgists (London), 1980, pp. 4/13-4/26.
- Page, K.; and Taylor, R. J.: Turbine Corrosion—Rig Evaluation and Engine Experience. Deposition and Corrosion in Gas Turbines, A. B. Hart and A. J. B. Cutler, eds., Halsted Press, 1973, pp. 350-375.
- McKee, D. W.; et al.: Effects of Fuel Impurities on the Hot Corrosion of Turbine Alloys. Presented at the 3rd Conference on Gas Turbine Materials in a Marine Environment (Bath, England), Sept. 20-23, 1976.
- Tasker, F. J. D.; Harris, C. W.; and Musgrave, N. S.: Corrosion Experience in the CEGB Gas Generators. Deposition and Corrosion in Gas Turbines, A. B. Hart and A. J. B. Cutler, eds., Halsted Press, 1973, pp. 385-408.
- Fryxell, R. E.; and Bessen, I. I.: Coating Life Assessment in Gas Turbines Operated for Ship Propulsion. Proceedings of the 1974 Gas Turbine Materials in the Marine Environment Conference, John W. Fairbanks and Irving Machlin, eds., MCIC Report 75-27, 1975, pp. 259-276.
- Hawkins, P. F.: LM 2500 Operating Experience on GTS Callaghan. Proceedings of the 4th Conference on Gas Turbine Materials in a Marine Environment, vol. II, U.S. Naval Sea Systems Command, 1979, pp. 49-68.
- DeCorso, S. M.; and Vermes, G.: Description of Program to Develop Combustion Turbine Design Guidelines Based on Deposition/Corrosion Considerations. Proceedings of the First Conference on Advanced Materials for Alternative-Fuel-Capable Directly Fired Heat Engines. John W. Fairbanks and John Stringer, eds., CONF-790749, 1979, pp. 287-300.
- Mom, A. J. A.: Environmental Testing of Coatings for Gas Turbines. Behavior of High Temperature Alloys in Aggressive Environments, I. Kirman et al., eds., The Metals Society (London), 1979, pp. 363-374.
- Hancock, P.: The Use of Laboratory and Rig Tests to Simulate Gas Turbine Corrosion Problems. Corros. Sci., vol. 22, no. 1, 1982, pp. 51-65.
- Shaw, T. R.; and Lutje-Schiphof, R. M.: The Royal Navy's Experience of Blade Corrosion During Engine Tests of Marine Gas Engines. Proceedings of the 1974 Gas Turbine Materials in the Marine Environment Conference, John W. Fairbanks and Irving Machlin, eds., MCIC Report 75-27, 1975, p. 31.
- Schultz, J. W.; and Hulsizer, W. R.: Corrosion-Resistant Nickel-Base Alloys for Gas Turbines. Met. Eng. Q., vol. 16, no. 3, Aug. 1976, pp. 15-24.
- Condé, J. F. G.; and Booth, G. C.: The Assessment of Hot Corrosion Resistance by Rig Testing—Philosophy and Experience. Deposition and Corrosion in Gas Turbines, A. B. Hart and A. J. B. Cutler, eds., Halsted Press, 1973, pp. 278-293.
- Felix, P. C.: Evaluation of Gas Turbine Materials by Corrosion Rig Tests. Deposition and Corrosion in Gas Turbines, A. B. Hart and A. J. B. Cutler, eds., Halsted Press, 1973, pp. 331-349.
- von E. Doering, H.; and Bergman, P.: Construction and Operation of a Hot Corrosion Test Facility. Mater. Res. Stand., vol. 9, no. 2, Sept. 1969, pp. 35-40.
- Foster, A. D.; von E. Doering, H.; and Hickley, J. W.: Fuel Flexibility in G. E. Gas Turbines. GER-2222L, General Electric, 1977.
- Buckland, B. O.; Foster, A. D.; and Treanor, J. J.: The Life of Gas Turbine Parts as Limited by Elevated Temperature Corrosion. Presented at the National Association of Corrosion Engineers Annual Meeting (Miami, Florida), Apr. 21, 1966.
- Rentz, W. A.; Freeman, W. R., Jr.; and Walters, J. J.: A Dynamic Hot-Corrosion Rig Testing Procedure. J. Mater., vol. 4, no. 3, Sept. 1969, pp. 520-539.
- Lee, S. Y.; DeCorso, S. M.; and Young, W. E.: Laboratory Procedures for Evaluating High-Temperature Corrosion Resistance of Gas Turbine Alloys. J. Eng. Power, vol. 93, no. 3, July 1971, pp. 313-320.
- Hot Corrosion in Gas Turbines. NMAB-260, National Materials Advisory Board, May 1970. (AD-870745.)
- Lowell, C. E.; Sidik, S. M.; and Deadmore, D. L.: High Temperature Alkali Corrosion in High Velocity Gases. DOE/NASA/2593-26, NASA TM-82591, 1981.
- Stringer, J.: Hot Corrosion of High Temperature Alloys. Symposium on Properties of High Temperature Alloys with

- Emphasis on Environmental Effects, Z. A. Foroulis and F. S. Pettit, eds., Electrochemical Society, Inc., 1976, pp. 513-556.
35. Barkalow, R. H.; and Pettit, F. S.: On the Mechanism for Hot Corrosion of CoCrAlY Coatings in Marine Gas Turbines. Proceedings of the 4th Conference on Gas Turbine Materials in a Marine Environment, vol. I, U.S. Naval Sea Systems Command, 1979, pp. 493-524.
 36. Kohl, Fred J.; et al.: Theoretical and Experimental Studies of the Deposition of Na_2SO_4 from Seeded Combustion Gases. J. Electrochem. Soc. vol. 126, no. 6, June 1979, pp. 1054-1061.
 37. Rosner, D. E.: Thermal (Soret) Diffusing Effects on Interfacial Mass Transport Rates. PCH PhysicoChemical Hydrodynamics, vol. 1, no. 2-3, 1980, pp. 159-185.
 38. Rosner, D. E.; et al.: Chemically Frozen Multicomponent Boundary Layer Theory of Salt and/or Ash Deposition Rates from Combustion Gases. Combust. Sci. Technol., vol. 20, no. 3-4, 1979, pp. 87-106.
 39. Gökoğlu, S. A. and Rosner, D. E.: Correlation of Thermophoretically Modified Small Particle Deposition Rates in Forced Convection Systems with Variable Properties, Transpiration Cooling and/or Viscous Dissipation. Int. J. Heat Mass Transfer. (In press, 1984.)
 40. Rosner, D. E.; and De La Mora, J. F.: Recent Advances in the Theory of Salt/Ash Deposition in Combustion Systems. Proceedings of the First Conference on Advanced Materials for Alternative-Fuel-Capable Directly Fired Heat Engines, John W. Fairbanks and John Stringer, eds., CONF-790749, 1979, pp. 301-330.
 41. Rosner, D. E.; et al.: Transport, Thermodynamics and Kinetic Aspects of Salt/Ash Deposition Rates from Combustion Gases. Characterization of High Temperature Vapors and Gases, J. W. Hastle, ed., NBS Spec. Publ. 561/2, U.S. National Bureau of Standards, 1979, pp. 1451-1476.
 42. Rosner, D. E.; and Atkins, R. M.: Experimental Studies of Salt/Ash Deposition Rates from Combustion Products Using Optical Techniques. Presented at the International Conference on Experimental Research into Fouling and Slagging Due to Impurities in Combustion Gases (Henniker, New Hampshire), July 12-17, 1981.
 43. Santoro, G. J.; et al.: Deposition and Material Response from Mach 0.3 Burner Rig Combustion of SRC-II Fuels. DOE/NASA/2593-20, NASA TM-81634, 1980.
 44. Gökoğlu, S. A.; Chen, B. K.; and Rosner, D. E.: Computer Program for the Calculation of Multicomponent Convective Diffusion Deposition Rates from Chemically Frozen Boundary Layer Theory. NASA CR-168329, 1984.
 45. Gordon, S.; and McBride, B. J.: Computer Program for Calculation of Complex Chemical Equilibrium Compositions, Rocket Performance, Incident and Reflected Shocks, and Chapman-Jouguet Detonations. NASA SP-273, 1971.
 46. Rosner, Daniel E.; and Nagarajan, R.: Transport-Induced Shifts in Condensate Dew-Point and Composition in High Temperature Multicomponent Systems with Chemical Reaction. Chemical Engineering Science (Pergamon Press, Ltd., Oxford). (In press, 1984.)
 47. Stecura, S.: Two-Layer Thermal Barrier Coating for High Temperature Components. Am. Ceram. Soc. Bull., vol. 56, no. 12, Dec. 1977, pp. 1082-1086.
 48. Gökoğlu, S. A.; and Rosner, D. E.: Note on the "Windward Fraction" of the Total Mass/Heat Transport for Flow Past a Circular Cylinder. Aerosol Sci. Tech., vol. 2, no. 4, 1983, pp. 543-544, Dec. 1983.
 49. Swithenbank, J.; et al.: A Laser Diagnostic Technique for the Measurement of Droplet and Particle Size Distribution. Experimental Diagnostics in Gas Phase Combustion Systems, B. T. Zinn, and C. T. Bowman, eds., Progress in Astronautics and Aeronautics, vol. 53, AIAA, 1977, pp. 421-447.
 50. Weiner, B. B.: Particle and Spray Sizing Using Laser Diffraction. Optics in Quality Assurance II, H. L. Kasdan, ed., Proc. SPIE, vol. 170, Society of Photo-optical Instrumentation Engineers, 1979, pp. 53-62.
 51. Poferl, D. J.; and Svehla, R. A.: Thermodynamic and Transport Properties of Air and Its Products of Combustion with ASTM-A-1 Fuel and Natural Gas at 20, 30, and 40 Atmospheres. NASA TN D-7488, 1973.
 52. Smith, M. C. G.: A Theoretical Note upon the Mechanism of Deposition in Turbine Blade Fouling. NGTE-M-145, National Gas Turbine Establishment, Feb. 1952. (AD-144890.)
 53. Hedley, A. B.; Brown, T. D.; and Shuttleworth, A.: Available Mechanisms for Deposition from a Combustion Gas Stream. ASME Paper 65 WA/CD-4, Nov. 1965.
 54. Jackson, P. J.: Deposition of Inorganic Materials in Oil-Fired Boilers. Ash Deposits and Corrosion Due to Impurities in Combustion Gases, R. W. Bryers, ed., Hemisphere Publishing Corp., 1978, pp. 147-161.
 55. Vermes, G.: Thermophoresis-Enhanced Deposition Rates in Combustion Turbine Blade Passages. J. Eng. Power, vol. 101, no. 4, Oct., 1979, pp. 542-548.
 56. McCreath, C. G.: The Fate of Sea Salt in a Marine Gas Turbine. Presented at the 3rd Conference on Gas Turbine Materials in a Marine Environment (Bath, England), Sept. 20-23, 1976.
 57. Ross, K.: Condensation of Sulphuric Acid from Flue Gas on a Cooled Cylinder. J. Inst. Fuel, vol. 38, no. 293, 1965, pp. 273-277.
 58. Fielder, W. L.; Stearns, C. A.; and Kohl, F. J.: Reactions of NaCl with Gaseous SO_3 , SO_2 and O_2 , Presented at the Electrochemical Society Spring Meeting, May 1983.
 59. Deadmore, D. L.; and Lowell, C. E.: Effect of Impurities in Coal-Derived Liquids on Accelerated Hot Corrosion of Superalloys. DOE/NASA/2593-79/13, NASA TM-81384, 1980.
 60. Santoro, G. J.: Hot Corrosion of Four Superalloys: HA-188, S-57, IN-617, and TD-NiCrAl. Oxid. Met., vol. 13, no. 5, 1979, pp. 405-435.
 61. Lowell, C. E.; and Deadmore, D. L.: The Kinetics of High Velocity, High Temperature Corrosion of U-700. Presented at the Electrochemical Society Fall Meeting (Detroit, Mich.), Oct. 17-21, 1982.
 62. Fang, W. C.; and Shores, D. A.: The Effect of Salt Deposit Thickness on Hot Corrosion Rates. Presented at the Electrochemical Society Fall Meeting (Los Angeles, Calif.), Oct. 14-19, 1979.
 63. Rosner, D. E.; Güneş, D.; and Anous, N.: Aerodynamically-Driven Condensate Layer Thickness Distribution of Isothermal Cylindrical Surfaces. Chemical Engineering Communications, vol. 24, Dec. 1983, pp. 275-287.
 64. Helt, J. E.: Evaluation of Alkali Metal Sulfate Dew Point Measurement for Detection of Hot Corrosion Conditions in PFBC Flue Gas. ANL/CEN/FE-80-12, Argonne National Laboratory, Nov. 1980.
 65. Bird, R. B.; Stewart, W. E.; and Lightfoot, E. N.: Transport Phenomena, John Wiley & Sons, 1960.
 66. Svehla, R. A.: Estimated Viscosities and Thermal Conductivities of Gases at High Temperatures. NASA TR R-132, 1962.
 67. Rosner, D. E.; Gökoğlu, S. A.; and Israel, R.: Rational Engineering Correlations of Diffusional and Inertial Particle Deposition Behavior in Non-Isothermal Forced Convection Environments. Proc. Engineering Foundation International Conference on the Fouling of Heat Exchange Surfaces. White Haven, Pa, Oct. 31-Nov. 5, 1982.
 68. Serafini, J. S.: Impingement of Water Droplets on Wedges and Double-Wedge Airfoils at Supersonic Speeds. NACA Report-1159, 1954.

TABLE I. - SYNTHETIC
SEA SALT
COMPOSITION

[ASTM D-1141-52
standard.]

Compound	Concentration, wt%
NaCl	68.066
MgCl ₂	14.422
Na ₂ SO ₄	11.346
CaCl ₂	3.218
KCl	1.914
NaHCO ₃	.555
KBr	.277
H ₃ BO ₃	.083
SrCl ₂	.111
NaF	.008

TABLE II. - CFBL COMPUTER PROGRAM INPUT DATA AND RESULTS FOR PRINCIPAL TESTS
USING COLLAR LINERS

	Species					
	Na ₂ SO ₄	Sea salt	K ₂ SO ₄	K ₂ SO ₄ (preheated air)	NaCl (preheated air)	NaNO ₃ (preheated air)
Airflow, kg/hr (lb/hr)	72.1 (158.9)	73.6 (162.2)	71.0 (156.3)	68.4 (150.7)	67.0 (147.6)	66.8 (147.2)
Inlet air temperature, K	298	298	298	526	532	532
Fuel-to-air ratio	0.0481	0.0465	0.0503	0.0503	0.0465	0.0466
Sulfur concentration in fuel, percent	0.052	0.052	0.044	0.053	0.048	0.061
Salt concentration in air, ppm (weight)	18.7	22.7	21.9	23.3	17.0	23.2
Na (K) concentration in air, ppm (moles)	7.6	8.6	7.2	7.7	8.4	7.9
Adiabatic temperature, T_A , K	1886	1845	1940	2085	2001	2003
Stagnation temperature, ($T_0 =$ $T_A - 150$ deg C) ^a , K	1736	1695	1790	1935	1851	1853
Dewpoint temperature ^b , K	1310	1255	1256	1260	1262	1312
Plateau deposition rate (experi- mental), \dot{m} , mg/hr	26.9 ± 2.7	17.6 ± 2.0	~ 21.0	21.8 ± 2.6	12.9 ± 1.8	15.8 ± 3.3
Plateau deposition rate (CFBL), \dot{m} , mg/hr	11.7	13.5	14.0	14.8	12.5	11.8
Difference between experimental and CFBL plateau deposition rates, percent	57	23	33	32	3	25

^aActual combustion gas temperatures averaged 150 deg C below the adiabatic temperatures calculated from fuel-to-air ratios.

^bCalculated by using CEC code (ref. 45).

TABLE III. - THERMAL BARRIER COATING SPECIFICATION^a

Materials	Procedures	Collector	Bond coat		Barrier coat	
			Coating thickness			
			mm	mils	mm	mils
Substrate: 304 Stainless steel (see fig. 27 for dimensions) Bond coat: Fe-35.4Cr-11.4Al-0.26Yb (in wt%) Barrier coat: ZrO ₂ -6Y ₂ O ₃ (in wt%)	Substrate: Surface to be coated was grit blasted (inserts that fit into ceramic spacers were taped, fig. 5(b)) Bond coat: Plasma sprayed in argon at 400 A and 12 kW. Barrier coat: Plasma sprayed in argon at 500 A and 12 kW.	A	0.25	10	0.23	9
		B	.36	14	.36	14

^aPrivate communication from Stephan Secura of NASA Lewis.TABLE IV. - CHARACTERISTICS OF DEPOSITION FOR SPECTRUM OF PARTICLE SIZES^a

Particle size range ^b , nm	Mass transport mode	Deposition species	Transport mechanism	Deposition characteristic ^c
0.1-1	Vapor diffusion	Atoms and molecules	Fick, Soret, and eddy diffusion	$T_{dp} < T_{\infty}$; low η and deposition on side away from line of sight; low sensitivity to $T_{\infty} - T_w$; and rate levels off for $T_w < T_{dp}$
1-10 ³	Vapor diffusion transition	Heavy molecules (condensate aerosols, clusters, and sub-micrometer particles)	Brownian and eddy diffusion and thermophoresis	$T_{dp} = T_{\infty}$; lowest η ; high sensitivity to $T_{\infty} - T_w$; and rate nearly linear with $T_{\infty} - T_w$
10 ³ -10 ⁵	Inertial	Macroscopic particles	Inertial and eddy impaction	No apparent T_{dp} ; highest η ; independent of $T_{\infty} - T_w$; preferential deposition on side facing flow

^aFrom ref. 9.^bMode of deposition is not fixed by particle size alone.^c η = capture efficiency of collector; T_{dp} = dewpoint temperature; T_{∞} = gas main-stream temperature; T_w = wall temperature.

TABLE V. – CALCULATED VALUES OF FICK DIFFUSION COEFFICIENT
FOR DEPOSITION FROM Na₂SO₄-SEEDED BURNER

Species	Molecular weight	Size parameter, σ , nm	Energy well depth parameter, ϵ/k , K	Collision integral, $\Omega_{D,i,mix,\infty}$	Fick diffusion coefficient for species i , $D_{i,mix,\infty}$, cm ² /sec
Na	22.9898	0.3567	1375	0.8534	3.3462
NaOH	40.00	.3804	1962	.8874	2.6347
Na ₂ SO ₄	142.06	.5	2221	.9004	1.6105
Combustion air (air)	28.816	.3617	97.0 ^a	-----	-----

^aFrom ref. 65; that calculated from ref. 66 is 78.6 K.

TABLE VI. – TRANSPORT NUMBERS FOR DEPOSITION FROM Na₂SO₄-SEEDED BURNER WITH CORRESPONDING WEIGHT FRACTION OF EACH SPECIES AT BOUNDARY LAYER INTERFACES AND FLUXES

	Reynolds number		
	Re = 1.3265×10^4	Re ^{1/2} = 115.1738	Re ^{2/3} = 560.3656
	Species		
	Na	NaOH	Na ₂ SO ₄
Fick diffusion coefficient for species i , $D_{i,mix,\infty}$, cm ² /sec	3.3462	2.6347	1.6105
Schmidt number of species i , Sc_i	0.8669	1.1010	1.8012
$Sc_i^{0.4}$	0.9445	1.0392	1.2654
Mass transfer Nusselt number for species i , $Nu_{m,i}$	73.32	80.67	98.23
Mass fraction of species i at outer edge of boundary layer, $\omega_{i,\infty}$	2.6591×10^{-7}	9.2867×10^{-6}	3.5318×10^{-11}
Mass fraction of species i at wall side of boundary layer, $\omega_{i,w}$	2.4956×10^{-20}	9.6929×10^{-14}	1.7777×10^{-11}
Diffusion mass flux of species i at collector side wall of boundary layer, $-j_{i,w}^*$, g/cm ² -sec	7.0212×10^{-9}	2.1242×10^{-7}	2.9865×10^{-13}
Mass fraction of sodium in species i , $\omega_{Na/i}$	1	0.575	0.324

TABLE VII. - PARAMETRIC SENSITIVITY RESULTS FOR
 Na_2SO_4 -SEEDED RUN WITH PROPERTY
 PARAMETERS LISTED

Quantity, q	Ratio of fractional change in deposition rate to fractional change in q , S_q
Mass fraction of sodium at outer edge of of boundary layer, $\omega_{\text{Na},\infty}$, 17.8 ppmw (com- bustion air)	1.07
Total mass flow rate, $\dot{m}(1+f)$, 72.1 kg/hr (158.9 lb/hr)	0.682
Mass fuel-to-air ratio, f , 0.0481	-----
Main-stream stagnation temperature, T_0 , 1980 K	0.297
Temperature at collector wall, T_w , 900 K	0.0443
NaOH collision diameter, $\sigma(\text{NaOH})$, 0.3804 nm (3.804 Å)	-0.5
NaOH energy well, $\epsilon(\text{NaOH})/k$, 1962 K	-0.0462

1. Report No. NASA TP-2225		2. Government Accession No.		3. Recipient's Catalog No.	
4. Title and Subtitle Experimental and Theoretical Deposition Rates From Salt-Seeded Combustion Gases of a Mach 0.3 Burner Rig				5. Report Date March 1984	
				6. Performing Organization Code 505-33-1A	
7. Author(s) Gilbert J. Santoro, Fred J. Kohl, Carl A. Stearns, Süleyman A. Gökoğlu, and Daniel E. Rosner				8. Performing Organization Report No. E-1752	
				10. Work Unit No.	
9. Performing Organization Name and Address National Aeronautics and Space Administration Lewis Research Center Cleveland, Ohio 44135				11. Contract or Grant No.	
				13. Type of Report and Period Covered Technical Paper	
12. Sponsoring Agency Name and Address National Aeronautics and Space Administration Washington, D.C. 20546				14. Sponsoring Agency Code	
15. Supplementary Notes Gilbert J. Santoro, Fred J. Kohl, and Carl A. Stearns, Lewis Research Center; Süleyman A. Gökoğlu, Analox Corporation, Cleveland, Ohio (work done under NASA Contract NAS3-23293); Daniel E. Rosner, Yale University, New Haven, Conn. (work done under NASA grant NAG3-201).					
16. Abstract Deposition rates on platinum-rhodium cylindrical collectors rotating in the cross streams of the combustion gases of a salt-seeded Mach 0.3 burner rig were determined. The collectors were internally air cooled so that their surface temperatures could be widely varied while they were exposed to constant combustion gas temperatures. The deposition rates were compared with those predicted by the chemically frozen boundary layer (CFBL) computer program, which is based on multi-component vapor transport through the boundary layer. Excellent agreement was obtained between theory and experiment for the NaCl-seeded case, but the agreement lessened as the seed was changed to synthetic sea salt, NaNO_3 , and K_2SO_4 , respectively, and was particularly poor in the case of Na_2SO_4 . However, when inertial impaction was assumed to be the deposition mechanism for the Na_2SO_4 case, the predicted rates agreed well with the experimental rates. The former were calculated from a mean particle diameter that was derived from the measured initial droplet size distribution of the solution spray. Critical experiments showed that liquid-phase deposits were blown off the smooth surface of the platinum-rhodium collectors by the aerodynamic shear forces of the high-velocity combustion gases but that rough or porous surfaces retained their liquid deposits.					
17. Key Words (Suggested by Author(s)) Deposition Mass and heat transfer Boundary layer Hot corrosion Combustion			18. Distribution Statement Unclassified - unlimited STAR Category 34		
19. Security Classif. (of this report) Unclassified		20. Security Classif. (of this page) Unclassified		21. No. of pages 46	
				22. Price* A03	

National Aeronautics and
Space Administration

Washington, D.C.
20546

Official Business

Penalty for Private Use, \$300

THIRD-CLASS BULK RATE

Postage and Fees Paid
National Aeronautics and
Space Administration
NASA-451



S I IJ,D, 840221 500903DS
DEPT OF THE AIR FORCE
AF WEAPONS LABORATORY
ATTN: TECHNICAL LIBRARY (SUL)
KIRTLAND AFB NM 37117

NASA

POSTMASTER:

If Undeliverable (Section 158
Postal Manual) Do Not Return